A&A 676, A103 (2023)
https://doi.org/10.1051/0004-6361/202245646

Astronomy & Astrophysics

Compton-thick AGN in the *NuSTAR* Era X: Analysing seven local CT-AGN candidates

D. Sengupta[1,2], S. Marchesi[1,2,3], C. Vignali[1,2], N. Torres-Albà[3], E. Bertola[1,2], A. Pizzetti[3], G. Lanzuisi[2], F. Salvestrini[4], X. Zhao[5], M. Gaspari[10], R. Gilli[2], A. Comastri[2], A. Traina[1,2], F. Tombesi[6,7,8,9], R. Silver[3], F. Pozzi[1], and M. Ajello[3]

[1] Dipartimento di Fisica e Astronomia (DIFA), Universitá di Bologna, via Gobetti 93/2, 40129 Bologna, Italy
e-mail: dhrubojyoti.sengupt2@unibo.it
[2] INAF-Osservatorio di Astrofisica e Scienza dello Spazio (OAS), via Gobetti 93/3, 40129 Bologna, Italy
e-mail: stefano.marchesi@inaf.it
[3] Department of Physics and Astronomy, Clemson University, Kinard Lab of Physics, Clemson, SC 29634, USA
[4] INAF – Osservatorio Astrofisico di Arcetri, Largo E. Fermi 5, 50125 Firenze, Italy
[5] Center for Astrophysics, Harvard & Smithsonian, 60 Garden Street, Cambridge, MA 02138, USA
[6] Department of Physics, Tor Vergata University of Rome, Via della Ricerca Scientifica 1, 00133 Rome, Italy
[7] INAF – Astronomical Observatory of Rome, Via Frascati 33, 00040 Monte Porzio Catone, Italy
[8] Department of Astronomy, University of Maryland, College Park, MD 20742, USA
[9] NASA Goddard Space Flight Center, Greenbelt, MD 20771, USA
[10] Department of Astrophysical Sciences, Princeton University, Princeton, NJ 08544, USA

Received 7 December 2022 / Accepted 2 May 2023

ABSTRACT

Context. We present the broad-band X-ray spectral analysis (0.6–50 keV) of seven Compton-thick active galactic nuclei (CT-AGN; line-of-sight (LOS) column density $>10^{24}$ cm^{-2}) candidates selected from the *Swift*-BAT 100 month catalogue using archival *NuSTAR* data.
Aims. We aim to obtain a complete census of the heavily obscured AGN in the local Universe ($z < 0.05$).
Methods. This work is in continuation of the ongoing research of the Clemson-INAF group to classify CT-AGN candidates at redshift $z < 0.05$ using physically motivated torus models.
Results. Our results confirm that three out of seven targets are bona fide CT-AGN. Adding our results to the previously analysed sources using *NuSTAR* data, we increase the population of bona fide CT-AGN by ∼9%, bringing the total number to 35 out of 414 AGN. We also performed a comparative study using `MYTorus` and `borus02` on the spectra in our sample, finding that both physical models are strongly consistent in the parameter space of LOS column density and photon index. Furthermore, we also investigate the clumpiness of the torus clouds by separately computing the LOS and average torus column densities in each of the seven sources. Adding our results to all the previous 48 CT-AGN candidates analysed by the Clemson-INAF research team for which *NuSTAR* observations are available, we find that 78% of the sources are likely to have a clumpy distribution of the obscuring material surrounding the accreting supermassive black hole.

Key words. galaxies: active – X-rays: galaxies – galaxies: Seyfert

1. Introduction

Diffuse X-ray emission from the central regions of accreting supermassive black holes in active galactic nuclei (AGN) is responsible for most of the cosmic X-ray background (CXB) radiation from a few keV to a few hundred keV (Comastri 2004; Gilli et al. 2007; Ueda et al. 2014). The contribution of unobscured AGN to the CXB is almost completely resolved into point-like sources at $E < 10$ keV (Worsley et al. 2005; Hickox & Markevitch 2006). Compton-thick AGN (CT-AGN; i.e. line-of-sight (LOS) column density $>10^{24}$ cm^{-2}) significantly contribute (∼15−30% Gilli et al. 2007; Ananna et al. 2019) to the CXB around its peak (∼20−30 keV; Ajello et al. 2008). In the local Universe ($z \leq 0.1$), the fraction of CT-AGN revealed by the X-ray observations is found to be ∼5%−10% (Vasudevan et al. 2013; Ricci et al. 2015; Torres-Albà et al. 2021). This reveals a large discrepancy with the predictions of AGN population synthesis models, which postulate that the fraction of local CT-AGN should be of ∼20%−50% (Ueda et al. 2014; Ananna et al. 2019) to model the CXB properly.

For low-redshift AGN, the circum-nuclear dusty torus clouds are considered as the dominant medium of obscuration; that is, obscuration from the interstellar medium (ISM) of the host galaxy is expected to be less significant (e.g., Gilli et al. 2022). Due to significant suppression of intrinsic X-rays below 10 keV by these obscuring Compton-thick clouds, it is difficult to detect heavily obscured AGN at $z \sim 0$ in the soft X-ray ($E < 10$ keV) band. As heavily obscured AGN have a noticeable Compton hump at ∼20−40 keV, hard X-ray ($E > 10$ keV) observatories allow the detection and characterisation of these kinds of sources at $z \sim 0$. For example, the *Swift* Burst Alert Telescope (BAT) is used as it is less biased against CT-AGN sources, being sensitive in the 15–150 keV range. To determine the existing CT-AGN fraction, using a BAT volume-limited sample is among the most efficient ways to reduce the bias against the obscured sources. The importance of an obscuring medium surrounding the meso

scale (∼1−100 pc) around AGN has been highlighted by several theoretical and numerical investigations (Gaspari et al. 2020, for a review). Briefly, in realistic turbulent environments, the host diffuse medium is expected to recurrently condense in a top-down multi-phase condensation cascade of warm and cold clouds, which then rain onto the central AGN. Such chaotic cold accretion (CCA; Gaspari et al. 2013) is therefore often responsible for a clumpy distribution at the meso scale, and boosts the feeding rates at the micro-scale (<1 pc). This multi-scale rain has been constrained and detected in a wide range of galaxies and AGN (e.g., Rose et al. 2019; Gaspari et al. 2019; Maccagni et al. 2021; Marchesi et al. 2022; McKinley et al. 2022; Temi et al. 2022).

The 100 month *Swift*-BAT catalogue[1] (the updated 150 month BAT catalogue is in preparation, Imam et al.) consists of 414 AGN at $z < 0.05$. From this AGN population, our Clemson-INAF research group[2] selected a sample of 55 CT-AGN candidates for which archival and Guest Observer observations with the Nuclear Spectroscopic Telescope Array are available (*NuSTAR*; Harrison et al. 2013). The target sources are observed by *NuSTAR* within the energy range of 3–79 keV with high sensitivity, because *NuSTAR* is the first instrument to focus X-ray photons at $E > 10$ keV. For the soft X-ray coverage at $E < 10$ keV, we used the available X-ray spectra from *XMM-Newton*, *Chandra*, or *Swift*-XRT. We carried out a systematic and comprehensive spectral analysis in 0.6−50 keV band on each of the 55 sources using the uniform torus models, `MYTorus` and `borus02` (see Marchesi et al. 2018; Zhao et al. 2021; Torres-Albà et al. 2021; Traina et al. 2021). In this work, we present the results of the last seven sources from this sample. Here, we independently computed LOS column density ($N_{\rm H,LOS}$) and average torus column density ($N_{\rm H,avr}$ or $N_{\rm H,tor}$) in order to study the clumpiness of the torus clouds even within the uniform torus framework. The $N_{\rm H,LOS}$ is derived from the absorbed powerlaw coming directly from the 'corona'. The $N_{\rm H,avr}$ is instead obtained from the reflection component, which can be modelled to derive the average properties of the obscuring medium, such as the above-mentioned average torus column density, the obscuring medium covering factor ($C_{\rm Tor}$), and its inclination angle ($\theta_{\rm Inc}$) with respect to the observer.

This paper is organised as follows: In Sect. 2, we discuss the selection methods and data analysis techniques. In Sect. 3, we present physically motivated torus models used in this work. Then, in Sect. 4, we show the results of each of the sources we analysed. In Section 5, we analyse and discuss our CT-AGN at $z < 0.05$, and display the current census of such objects, combining our results with those obtained in previous works. Finally, in Sect. 6, we present the conclusions and a brief summary of our work, and mention some possible future projects. In Appendices A and B, we show the tables of best-fit parameters and X-ray spectral fitting plots, respectively. All reported error ranges are at the 90% confidence level unless stating otherwise. Through the rest of the work, we assume a flat ΛCDM cosmology with $H_0 = 69.6\,{\rm km\,s^{-1}\,Mpc^{-1}}$, $\Omega_m = 0.29$, and $\Omega_\Lambda = 0.71$ (Bennett et al. 2014).

2. Sample selection and data reduction

The seven sources (see Table 1 for details) of our sample are CT-AGN candidates selected from the volume-limited sample of the *Swift*-BAT 100 month catalogue in the local Universe ($z < 0.05$, $D \lesssim 200$ Mpc). These Seyfert galaxies were previously classified as CT-AGN in Ricci et al. (2015) using the `BNtorus` model (Brightman & Nandra 2011), where *Swift*-XRT was used for $E < 10$ keV (except for ESO138-G001, where *XMM-Newton* data were used) and *Swift*-BAT for $E > 10$ keV. Instead of BAT observations (15–150 keV), we are using *NuSTAR* in the 3–50 keV range, as it is a grazing incidence telescope with lower background and a smaller field of view, resulting in excellent sensitivity to source detection with better photon statistics. At $E < 10$ keV, we preferred *XMM-Newton* or *Chandra* for better data quality, particularly in terms of source statistics compared to *Swift*-XRT. For NGC 2788A, only *Swift*-XRT data were available. The objects analysed in this work are CT-AGN candidates in the 100 month BAT sample for which no analysis with `MYTorus` or `borus02` of the joint soft X-ray and *NuSTAR* spectra have yet been published.

2.1. NuSTAR data reduction

We used both focal plane modules FPMA and FPMB of *NuSTAR* for each source. The collected data have been processed by *NuSTAR* Data Analysis Software– NUSTARDAS version 2.0.0. The raw event files are calibrated by the *nupipeline* script using the response file from the Calibration Database– CALDB version 20210202. The source and background spectra are extracted from 30″ (≈50% of the encircled energy fraction–EEF at 10 keV) and 50″ circular regions, respectively. Using *nuproducts* scripts, we generated source and background spectra files, along with response matrix files–RMF and ancillary response files–ARF. Finally, the *NuSTAR* spectra are grouped with at least 20 counts per bin using *grppha*. For each source, we used all the available *NuSTAR* observational data taken during different epochs in order to (a) check variability, and (b) improve the statistics of the spectra of these obscured sources between 3 and 50 keV.

2.2. XMM-Newton data reduction

In *XMM-Newton*, we collected the data from the PN, MOS1, and MOS2 detectors. Using SAS version 19.0.0, we processed the data using *epproc* and *emproc* for the PN and MOS filters, respectively. Finally, we reduced and cleaned the flares using *evselect*. The source photons were obtained from a 30″ circular region, with ∼85% EEF for EPIC-PN at 1.5 keV. Background spectra were extracted from a 50″ circle near the source. Each spectrum has been binned at 20 counts per bin using *grppha*. We prefer to use *XMM-Newton* wherever it is available, because the effective area of *XMM-Newton* in 0.3–10 keV is approximately ten times bigger than the *Swift*-XRT one and approximately two times bigger than the *Chandra* one.

2.3. Chandra data reduction

Although the effective area of *Chandra* is smaller than that of *XMM-Newton*, it is still five times larger than that of *Swift*-XRT. Also, *Chandra* shows better angular resolution, a lower background, and has a greater capacity to resolve extended emission from non-nuclear sources. We use *Chandra* in two different scenarios: (1) when *XMM-Newton* data are not available and (2) to improve the photon statistics at $E < 10$ keV when they are. CIAO version 4.13 is used to process and reduce the data. The source spectra are extracted using a circular region of 5″ radius, which includes >99% EEF.

[1] http://bat.ifc.inaf.it/100m_bat_catalog/100m_bat_catalog_v0.0.htm
[2] https://science.clemson.edu/ctagn/

Table 1. Observational details of each sources.

Source	AGN [(a)] Types	log flux [(b)] in erg cm^{-2} s^{-1}	Redshift (z)	Instrument	Sequence ObsID	Start time (UTC)	Exposure time (ks)	Net spectral counts [(c)]
MCG-02-12-017	Sy2 candidate	8.84	0.03246	*XMM-Newton*	0762920601	2016-03-01	30.0	753, 225, 270
				NuSTAR	60001160002	2014-11-28	34.0	441, 379
				NuSTAR	60101015002	2016-03-02	19.5	349, 369
NGC 4180	Sy2	17.58	0.00699	*Chandra*	9438	2008-11-16	2.1	6
				NuSTAR	60201038002	2016-07-14	23.4	429, 387
				NuSTAR	60160480002	2020-07-14	31.6	212, 212
NGC 2788A	Sy2	21.46	0.01335	*Swift*-XRT	[(*)]	2008—2020	17.8 [(d)]	34
				NuSTAR	60469001002	2019-06-14	27.6	608, 617
				NuSTAR	60160344002	2020-08-14	23.2	639, 530
NGC 1106	Sy2	15.49	0.01447	*XMM-Newton*	0821870301	2019-03-02	32.6	1129, 257, 422
				NuSTAR	60469002002	2019-02-22	18.7	285, 332
				NuSTAR	60160130002	2020-09-09	22.3	360, 354
ESO406-G004	Sy2	12.38	0.02897	*Chandra*	14050	2012-06-07	5.1	25
				NuSTAR	60201039002	2016-05-25	36.3	390, 357
				NuSTAR	60161799002	2020-06-26	23.7	120, 86
2MASX J20145928+2523010	Sy2	10.55	0.04422	*XMM-Newton*	0802450501	2017-11-18	44.8	5232, 1980, 1134
				Chandra	21299	2018-12-17	3.7	532
				NuSTAR	60201032002	2017-05-27	28.1	1252, 1137
				NuSTAR	60160731002	2020-04-21	9.4	608, 624
ESO138-G001	Sy2	19.46	0.00914	*XMM-Newton*	0690580101	2013-02-24	135.4	27058, 8878, 9016
				NuSTAR	60201040002	2016-05-22	45.7	3101, 2806
				NuSTAR	60061274002	2020-04-01	53.2	3463, 3328

Notes. [(a,b)]AGN types and log flux between 14 and 195 keV is reported from the 105 month BAT catalogue of Oh et al. (2018). Only for ESO406-G004 is the AGN type reported from Koss et al. (2016). [(c)]The reported *XMM-Newton* net counts (background-subtracted total source counts) are those of the PN, MOS1, and MOS2 modules for a radius of 30″ in 0.3–10 keV, respectively. The reported *NuSTAR* net counts are those of the FPMA and FPMB modules for a radius of 30″ between 3 and 50 keV, respectively. The reported *Chandra* net counts are for the ACIS-I detector for a radius of 5″ in 0.5–7 keV. The reported *Swift*-XRT net counts are for a radius of 12″ in 0.5–10 keV. [(d)]Total exposure time of all the *Swift*-XRT observations [(*)]Collection of the following ObsID- 00081038001, 00037312004, 00037312001, 00037312002, 00037312003, 03106140005, 03106140004, 03106140001, 03106140002, 07002346001, 07002347001.

3. Spectral modeling

For X-ray spectral fitting on the objects in our sample, we used `XSPEC` (Arnaud 1996) version 12.11.1 in HEASOFT. The metal abundance is fixed to solar metallicity from Anders & Grevesse (1989), while the photoelectric cross sections for all absorption components are obtained using the approach of Verner et al. (1996). The Galactic absorption column density is fixed for each source in our sample following Kalberla et al. (2005). We also used a thermal `mekal` (Mewe et al. 1985; Kaastra 1992; Liedahl et al. 1995) component to phenomenologically model the soft excess which is often observed in the spectra of obscured AGN.

We followed a standard approach to analyse the CT-AGN candidates –using self-consistent and up-to-date physically motivated uniform torus models– based on Monte Carlo simulations: `MYTorus` (Murphy & Yaqoob 2009; Yaqoob 2012) and `borus02` (Baloković et al. 2018), which are specifically developed to characterise the X-ray spectra of heavily obscured AGN. In this section, we describe how these two uniform torus models are used.

3.1. MyTorus

The obscuring material in `MYTorus` follows a toroidal or donut-like geometry, with circular cross-section. This model consists of three components: direct continuum (MYTZ), Compton-scattered continuum (MYTS), and a fluorescent line component (MYTL). The MYTZ, also called the zeroth-order component, models the attenuation of intrinsic X-ray radiation by the obscuring torus on the LOS of the observer. The second component, MYTS, computes the Compton-scattered photons, which are responsible for the Compton hump near ∼20−30 keV. Finally, MYTL models prominent fluorescent emission lines such as: Fe K$_\alpha$ and Fe K$_\beta$ around 6.4 keV and 7.06 keV, respectively. Following the techniques in Yaqoob (2012) and from the previous results of Marchesi et al. (2018, 2019a,b), Zhao et al. (2019a,b), Traina et al. (2021), Torres-Albà et al. (2021) and Silver et al. (2022), we used only the decoupled configuration of `MYTorus` to estimate the clumpiness of the torus clouds. Here, we calculated the column density from direct continuum ($N_{\rm H,z}$) and scattered continuum ($N_{\rm H,S}$) separately, allowing flexibility on the parameter estimation even within a uniform cloud distribution framework. The ratio $N_{\rm H,z}/N_{\rm H,S}$ is used to evaluate the clumpiness, depending on how far the ratio is from unity. In `XSPEC`, the configuration is as follows:

$$\begin{aligned}\text{Model MyTorus}_{\text{edge-on}} = C_{\rm Ins} \ * \ & phabs * \\ & (zpow * \text{MYTZ} + A_{S,90} * \text{MYTS} + A_{L,90} * \text{MYTL} + \\ & f_s * zpow + mekal + zgauss),\end{aligned} \quad (1)$$

$$\begin{aligned}\text{Model MyTorus}_{\text{face-on}} = C_{\rm Ins} \ * \ & phabs * \\ & (zpow * \text{MYTZ} + A_{S,0} * \text{MYTS} + A_{L,0} * \text{MYTL} + \\ & f_s * zpow + mekal + zgauss).\end{aligned} \quad (2)$$

Here, Eq. (1) models the edge-on view ($\theta_{\rm Inc} = 90°$) and Eq. (2) the face-on view ($\theta_{\rm Inc} = 0°$) of the AGN. We used both inclination angles to carry out a comparative study of the scattering

column density arising from the polar dust (edge-on) versus that from the back-reflection of the torus (face-on). We equated and fixed the relative normalisations from scattering and line components, $A_S = A_L = 1$, as we consider them to have originated from the same regions where the direct power-law emerged. $C_{\rm Ins}$ is a cross-calibration constant between the different instruments of telescopes (or a cross-normalization constant between different observations of the same telescopes). We also included some additional components: f_s to compute the scattering fraction from the direct power law that does not interact (or elastically interacts) with the torus, *mekal* to phenomenologically model the soft excess, and *zgauss* to include any additional emission lines.

3.2. BORUS02

The obscuring medium in `borus02` consists of a spherical geometry with biconical (polar) cut-out regions (Baloković et al. 2018). This model is composed of three components: (a) `borus02` itself, which is a reprocessed component (including Compton-scattered + fluorescent line component), (b) *zphabs* ∗ *cabs* to include LOS absorption with Compton scattering through the obscuring clouds; with this component we multiply a $cutoffpl_1$ to take into account the primary power-law continuum, and (c) finally another $cutoffpl_2$ component is included separately with f_s to include a scattered unabsorbed continuum. The significant difference between `borus02` and `MYTorus` is that the torus covering factor ($C_{\rm Tor}$) in this model is kept as a free parameter varying in the range of 0.1−1 (i.e. the torus opening angle is in the range of $\theta_{\rm Tor} = 0°-84°$), along with inclination angle $\theta_{\rm Inc}$, which is kept free between 18° and 87°. In our analysis using `XSPEC`, we used the following model configuration:

$$\begin{aligned}\text{Model borus02} = C_{\rm Ins} * phabs * (borus02 + zphabs \\ * cabs * cutoffpl_1 + f_s * cutoffpl_2 \\ + mekal + zgauss),\end{aligned} \quad (3)$$

where *mekal* is included to compute the soft excess below 1 keV, and *zgauss* is introduced if there is any emission line signature not included in `borus02`.

4. Results of the X-ray spectral analysis

In this section, we show the results of X-ray spectral fitting on each CT-AGN candidate from Ricci et al. (2015) using both physically motivated models mentioned in Sect. 3, with two versions of `MYTorus` and one `borus02`. Table 7 displays the summary of our analysis on the sample using `borus02`. The best-fit parameters are reported in Table 2 and in Appendix A. The plots with X-ray spectral fitting are shown in Figs. 1 and Appendix B. The background contribution for all these sources is within 20%, unless mentioned otherwise. The tables also report the observed flux and intrinsic luminosity for each source.

4.1. MCG-02-12-017

The source was marked as a CT-AGN candidate based on the data of *Swift*-XRT and *Swift*-BAT, with $\log N_{\rm H,LOS} = 24.25^{+1.06}_{-0.46}$ in $\rm cm^{-2}$. For our analysis, we used the quasi-simultaneous observations of *XMM-Newton* and *NuSTAR*, along with another *NuSTAR* observation taken about 15 months earlier with a longer exposure time of ∼34 ks. The cross-calibration ratio between *XMM-Newton* and the *NuSTAR* detector for quasi-simultaneous observations is ∼75%, whereas for the previous *NuSTAR* observation, this ratio is ∼85%.

Table 2. Summary of best-fit solutions of *XMM-Newton* and *NuSTAR* data using different models for MCG-02-12-017.

Model	MyTorus Edge-on	MyTorus Face-on	borus02
χ^2/d.o.f.	192/200	192/200	186/198
$C_{\rm Ins_1}$ [(a)]	$0.88^{+0.11}_{-0.10}$	$0.89^{+0.09}_{-0.08}$	$0.89^{+0.11}_{-0.10}$
$C_{\rm Ins_2}$ [(b)]	$1.24^{+0.16}_{-0.15}$	$1.28^{+0.12}_{-0.14}$	$1.25^{+0.17}_{-0.15}$
Γ	$1.94^{+0.14}_{-0.14}$	$1.98^{+0.06}_{-0.12}$	$2.11^{+0.13}_{-0.16}$
$C_{\rm Tor}$ [(c)]	–	–	$1.00^{+*}_{-0.35}$
$\theta_{\rm Inc}$ [(d)]	–	–	49^{+*}_{-*}
$N_{\rm H,z}$ [(e)]	$0.26^{+0.03}_{-0.03}$	$0.26^{+0.03}_{-0.02}$	$0.27^{+0.03}_{-0.03}$
$N_{\rm H,S}$ [(f)]	$2.00^{+2.83}_{-1.10}$	$10.0^{+*}_{-9.99}$	$1.98^{+1.07}_{-0.52}$
f_s [(g)] 10^{-2}	$0.25^{+0.16}_{-0.13}$	$0.17^{+0.09}_{-0.09}$	$0.20^{+0.12}_{-0.11}$
kT [(h)]	$0.46^{+0.41}_{-0.37}$	$0.48^{+0.29}_{-0.19}$	$0.47^{+0.49}_{-*}$
F [(i)]$_{2-10\,\rm keV}$	$5.65^{+0.40}_{-0.67}$	$5.59^{+0.44}_{-0.71}$	$5.55^{+0.45}_{-1.76}$
F [(j)]$_{10-40\,\rm keV}$	$1.57^{+0.11}_{-0.36}$	$1.65^{+0.34}_{-0.41}$	$1.63^{+0.17}_{-0.60}$
L [(k)]$_{2-10\,\rm keV}$	$4.98^{+2.13}_{-1.52}$	$4.82^{+0.56}_{-0.59}$	$5.17^{+1.89}_{-1.47}$
L [(l)]$_{10-40\,\rm keV}$	$4.69^{+2.01}_{-1.44}$	$4.27^{+0.51}_{-0.51}$	$3.77^{+1.37}_{-1.07}$

Notes. We summarise here the best-fits of joint *XMM-Newton–NuSTAR* spectra using different torus models at 0.6–50 keV. The statistics and degrees of freedom for each fit are also reported. [(a)]$C_{\rm Ins_1} = C_{\rm FPMA/PN}$ is the cross calibration constant between *NuSTAR* observation of 2014 and *XMM-Newton* observation of 2016. [(b)]$C_{\rm Ins_2} = C_{\rm FPMA/PN}$ is the cross calibration constant between *NuSTAR* observation of 2016 and *XMM-Newton* observation of 2016. [(c)]Covering factor: fraction of sky covered by the torus, as seen by the nucleus, given by $C_{\rm Tor} = \cos(\theta_{\rm Tor})$. [(d)]Inclination angle: angle (in degrees) between the symmetry axis of the torus and the LOS angle. [(e)]"Line of sight" column density in 10^{24} $\rm cm^{-2}$. [(f)]Average column density from scattering in 10^{24} $\rm cm^{-2}$. [(g)]Fraction of primary emission getting scattered, rather than absorbed by the obscuring material. [(h)]Temperature in the thermal component *mekal* in keV. [(i)]Flux between 2 and 10 keV in 10^{-13} erg $\rm cm^{-2}$ $\rm s^{-1}$. [(j)]Flux between 10 and 40 keV in 10^{-12} erg $\rm cm^{-2}$ $\rm s^{-1}$. [(k)]Intrinsic luminosity between 2 and 10 keV in 10^{42} erg $\rm s^{-1}$. [(l)]Intrinsic luminosity between 10 and 40 keV in 10^{42} erg $\rm s^{-1}$.

This source is very well fitted (see Table 2 and Fig. 1) by all three models. All the physically motivated models are in agreement that the observed LOS column density $N_{\rm H,LOS} = (0.23-0.30) \times 10^{24}$ $\rm cm^{-2}$ is Compton-thin, in disagreement with the Ricci et al. (2015) result. Even when we only used the quasi-simultaneous observations, the LOS column density is consistent with each other's observation having range $N_{\rm H,LOS,qs} = (0.24-0.32) \times 10^{24}$ $\rm cm^{-2}$. The average torus column density is instead found to be close to or above the Compton-thick threshold by `MYTorus` Edge-On and `borus02` ($N_{\rm H,tor} = (0.9-4.83) \times 10^{24}$ $\rm cm^{-2}$). The best-fit value of the photon index is found to be in range of $\Gamma = 1.94-2.11$, considering all the models. Estimation of the torus properties, such as covering factor and opening angle in `borus02`, is found to be difficult, because the reflection component is subdominant.

4.2. NGC 4180

This target was classified as a CT-AGN candidate based on the data of *Swift*-XRT and *Swift*-BAT, $\log N_{\rm H} = 24.15^{+0.27}_{-0.22}$ $\rm cm^{-2}$. For our analysis, we included only the two *NuSTAR* observations, excluding the *Chandra* observation due to its extremely

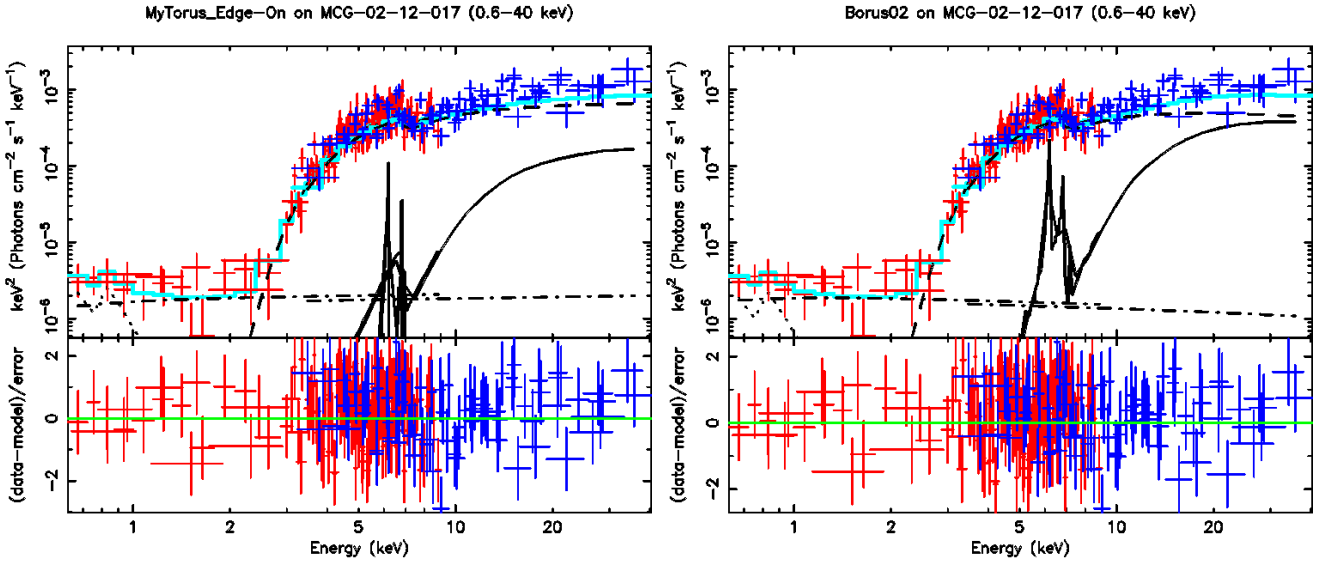

Fig. 1. X-ray spectral fitting of decoupled Edge-On `MYTorus` (*left*) and `borus02` (*right*) models of MCG-02-12-017 data. In both the plots, the soft X-ray data (from *XMM-Newton*) are marked in red and hard X-ray data (from *NuSTAR*) are marked in blue. The joint best-fit model in both soft and hard X-rays is plotted as a cyan line. The individual model components are shown as black lines as follows: direct power-law emission (dashed), reflected emission (solid), scattered emission (dot-dashed), iron line (solid; in `MYTorus` it is separate, in `borus02` it is included in reflected emission), and mekal (dotted).

poor photon statistic (Table 1). We used the Portable Interactive Multi-Mission Simulator[3] to convert the *NuSTAR* spectrum for $E > 2$ keV, and found the predicted count rate (1.56×10^{-3} cts s^{-1}) for *Chandra* to be within the error range of the observed count rate ($1.42 \pm 0.82 \times 10^{-3}$ cts s^{-1}). Moreover, the cross-normalisation ratio between two separate observations (2016 and 2020) of the FPMA detector is ∼50%, portraying noticeable variability of the source.

The source is very well fitted (see Table A.1 and Fig. B.3) by all models, with models showing consistent results with one other, giving Compton-thick LOS column density $N_{\rm H,LOS} = (1.25{-}6.10) \times 10^{24}$ cm^{-2} in agreement with the results obtained by Ricci et al. (2015). Even the average torus column density, which is more accurately constrained by `MYTorus` Edge-On and `borus02` in this case, shows $N_{\rm H,tor} = (0.66{-}4.56) \times 10^{24}$ cm^{-2}, suggesting a moderate CT nature of the obscuring material as a whole. The best-fit values of photon index are $\Gamma \sim 1.40{-}1.66$, considering all the models. The hard index value shows that the models might not be able to properly estimate the direct power-law component contribution in the absence of soft X-ray data, and therefore cannot fully break the $N_{\rm H,LOS}$–Γ degeneracy. For similar reasons, the covering factor and inclination angle also show a large range of uncertainty. However, as shown in Fig. B.3, the overall spectral emission is dominated by the reflected component over the LOS component. Therefore, from the available data, this source can be identified as a bona fide CT-AGN. However, soft X-ray observations would be required to put stronger constraints on the different obscuring material parameters.

4.3. NGC 2788A

This source was marked as a CT-AGN candidate based on the data of *Swift*-XRT and *Swift*-BAT, with log $N_{\rm H} = 25.55^{+*}_{-1.41}$ in cm^{-2}. For our analysis, we have two *NuSTAR* observations (taken in 2019 and 2020; total exposure ∼51 ks). To cover the <3 keV energy range, we make use of 12 *Swift*-XRT observations taken from 2008 to 2020[4]. Due to very low spectral counts in soft X-ray (∼34 counts; see Table 1), we grouped the spectra from XRT with 1 count/bin and jointly fitted the *Swift*-XRT and *NuSTAR* spectra applying C-statistics over the entire range in `XSPEC`. The cross-calibration variability between *Swift*-XRT and *NuSTAR* detectors fall within ∼20%.

This source is very well fitted using the physically motivated models (see Table A.2 and Fig. B.1). The results are consistent between all models. The LOS column density $N_{\rm H,LOS} = (1.67{-}2.36) \times 10^{24}$ cm^{-2} shows a CT column density, which validates the result of Ricci et al. (2015), although with a significantly lower value. In comparison with the average column density of the torus, the best-fit value of `MYTorus` Face-On and `borus02` are close to each other with the range $N_{\rm H,tor} = (1.72{-}22.69) \times 10^{24}$ cm^{-2}, agreeing with the CT nature of the cloud distribution. On these two models, the best-fit value of Γ is around 1.8–1.9. In addition, the `borus02` model best fits the data with an intermediate covering factor, although with large uncertainties ($0.49^{+0.47}_{-0.28}$) and inclination angles in the range 47°−72°. In Fig. B.1, both models show considerable dominance of the reflection component over the LOS component, even more strongly suggesting the CT nature of the source. From the available *NuSTAR* data, this source is confirmed to be a bona fide CT-AGN. However, further observations below 10 keV are needed for a better understanding of the properties of the obscuring material.

4.4. NGC 1106

This candidate was marked as a CT-AGN based on the data of *Swift*-XRT and *Swift*-BAT, which suggest a log $N_{\rm H} = 24.25^{+0.29}_{-0.17}$ in cm^{-2}. For our analysis, we used a *XMM-Newton* observation (taken in 03/2019; ∼33 ks) and *NuSTAR* observations (taken in 02-2019 and 09-2020; total exposure ∼41 ks).

[3] https://cxc.harvard.edu/toolkit/pimms.jsp

[4] We obtained a joint spectrum using the tool available at www.swift.ac.uk/user_objects/

The cross-calibration ratio between *XMM-Newton* and *NuSTAR* detectors is 1.4.

This source is very well fitted (see Table A.3 and Fig. B.2). All three models show consistent results. The LOS column density $N_{\rm H,LOS} = (2.83-5.73) \times 10^{24}$ cm^{-2} shows a CT column density, which validates the result of Ricci et al. (2015). The torus average column density is $N_{\rm H,tor} = (1.34-7.98) \times 10^{24}$ cm^{-2}, in agreement with the CT nature of the torus. It is also interesting to note that `borus02`, which has a better reduced χ^2 value (∼1.04) and a value of Γ (∼1.92) closer to the AGN average (Marchesi et al. 2016), also estimates that the LOS column density is in agreement with the average torus column density, suggesting that the obscuring material is likely uniform (see Table A.3). In addition, the `borus02` model gives a high covering factor ($0.87^{+0.11}_{-0.24}$), and moderate inclination angle in the range of 28°−74°. Figure B.2 shows how the reflection component is dominant over the direct power law. From the above analysis, this source can be counted as a bona fide CT-AGN.

4.5. ESO406-G004

This target was marked as a CT-AGN candidate based on the data of *Swift*-XRT and *Swift*-BAT, which suggest a log $N_{\rm H} = 24.74^{+*}_{-0.55}$ in cm^{-2}. For our analysis, we have a *Chandra* observation with very low exposure (∼5.1 ks) and only 25 spectral counts in soft X-rays. Furthermore, even though the two archival *NuSTAR* observations have a much higher exposure time (total ∼60 ks), the source count statistic is significantly lower than that of the other sources (∼747 net counts in 2016 and ∼206 net counts in 2020; see Table 1). Due to such low spectral counts, we used C-statistics to fit the data after binning with 1 count/bin in *Chandra*, and 10 counts/bin and 20 counts/bin on *NuSTAR* observations of 2020 and 2016, respectively. It is also noticeable that the observations were taken after large gaps (∼4 years), and the cross-calibration ratio between ACIS (of *Chandra*) and FMPA (of *NuSTAR*) detectors shows large variability: ∼1.3−1.7. Furthermore, in the *NuSTAR* observation of June 2020, the background-noise contribution on the spectral signal is ∼30%−40%, whereas the other data sets show contributions of <20%.

This source is very well fitted by all the models. All three models show consistent results. The LOS column density for this source of $N_{\rm H,LOS} = (0.59-1.28) \times 10^{24}$ cm^{-2} shows a mostly Compton-thin column density, contrary to the result of Ricci et al. (2015). The decoupled `MYTorus` estimates $N_{\rm H,tor} = (0.13-2.03) \times 10^{24}$ cm^{-2} and `borus02` estimates, with a large error range, $N_{\rm H,tor} = (0.11-5.01) \times 10^{24}$ cm^{-2}. Overall, the fit suggest mostly Compton-thin clouds with upper bounds crossing the CT threshold. Due to the lack of *XMM-Newton* data, it is likely that the low-statistic in the soft X-ray, along with a fairly low statistic in the hard X-rays, make it difficult to properly disentangle the Γ–$N_{\rm H,LOS}$ degeneracy. For similar reasons, we find that `borus02` computes a low covering factor (best-fit value ∼0.10) and a small inclination angle (18°) with a high or unconstrained error range.

Furthermore, we noticed a significant cross-calibration variability for the two *NuSTAR* observations (see Table A.4). We therefore also carried out a comparative study of the *NuSTAR* observations of this source taken in May 2016 and June 2020 in order to check flux and LOS column density variability (following the approach of Marchesi et al. 2022; Torres-Albà et al. 2023; Pizzetti et al. 2022); these are listed in Table 3. The cross-calibration flux value is measured with respect to the *Chandra* observation of June 2012. We fixed all the other parameters for these two *NuSTAR* observations to the best-fit values, and only kept the $N_{\rm H,LOS}$ and flux free to vary. We studied the variability by fixing one of the two parameters and leaving the other free to vary, and finally compared the values by varying both of them. We find that the $N_{\rm H,LOS}$ increases ∼53% from 2016 to 2020 and the flux is significantly increased (∼230%) in the 2020 observation with respect to the 2016 one. However, from the reduced C-stat value, we find that the residual (data-model) worsens if we vary only the LOS column density; whereas fixing the $N_{\rm H,LOS}$ does not significantly change the fit with respect to varying both flux and column density for the different *NuSTAR* epochs. This indicates that the variability observed between the two *NuSTAR* observations can be explained within a pure luminosity variability scenario, while the fit improvement is not significant when allowing the LOS column density to vary.

Table 3. Flux and column-density variability of ESO406-G004 from *NuSTAR* observations using `borus02`.

Parameter	Fixing only $N_{\rm H,LOS}$	Fixing only $C_{\rm Ins}$	Varying both
$C_{\rm Ins,NuS1}$ [(a)]	$0.77^{+0.15}_{-0.12}$	$0.84^{+0.22}_{-0.16}$	$0.82^{+0.18}_{-0.14}$
$C_{\rm Ins,NuS2}$ [(b)]	$0.35^{+0.08}_{-0.07}$	″	$0.25^{+0.13}_{-0.08}$
$N_{\rm H,LOS,NuS1}$ [(c)]	$0.82^{+0.15}_{-0.12}$	$0.88^{+0.21}_{-0.16}$	$0.86^{+0.17}_{-0.14}$
$N_{\rm H,LOS,NuS2}$ [(d)]	″	$1.88^{+0.78}_{-0.45}$	$0.58^{+0.29}_{-0.21}$
C-Stat/d.o.f.	84/93	92/93	82/92

Notes. [(a)]Cross-calibration value from FPMA detector, observed in 2020. [(b)]Cross-calibration value from FPMA detector, observed in 2016. [(c)]LOS column density from FPMA detector in 10^{24} cm^{-2}, observed in 2020. [(d)]LOS column density from FPMA detector in 10^{24} cm^{-2}, observed in 2016.

4.6. 2MASX J20145928+2523010

This candidate was also classified as a CT-AGN based on the data of *Swift*-XRT and *Swift*-BAT, which suggest log $N_{\rm H} = 24.42^{+0.20}_{-0.17}$ in cm^{-2}. For our analysis, we have *Chandra* (taken in 12/2018) and *XMM-Newton* (taken in 11/2017) spectra with excellent photon statistics in the 0.6−10 keV energy range (total spectral counts ∼9k). Even in hard X-rays, the two archival *NuSTAR* observations (taken in May 2017 and April 2020) have a high exposure time and net spectral counts (total ∼3.6k). It is worth noting that for the joint *NuSTAR* and *XMM-Newton* observation taken in 2017, we measure a cross-calibration ratio of <1.4. However, the flux values of the 2018 *Chandra* and the 2020 *NuSTAR* observations are almost twice (∼1.93−2.15) that of the 2017 *XMM-Newton* observation. There is also significant flux variability (factor of 0.77) between the *NuSTAR* and *XMM-Newton* observations taken only 6 months apart.

This source is very well fitted by all the models (see Table A.5). All three models show consistent results. The LOS column density for this source is $N_{\rm H,LOS} = (1.86-2.29) \times 10^{22}$ cm^{-2}, with a fairly low LOS column density just above the standard 10^{22} cm^{-2} threshold used to classify obscured AGN. Such a result is in strong disagreement with that of Ricci et al. (2015). Even the average column density of the torus is $N_{\rm H,tor} = (9.07-28.66) \times 10^{22}$ cm^{-2}, that is, Compton-thin. The decoupled `MYTorus`model shows a better estimate of the photon index ∼1.69−1.89 compared to `borus02`, in terms of consistency with the expected value. Due to strong domination of the intrinsic power law over the reflection component in the hard X-ray

Table 4. Flux and column-density variability of 2MASX J20145928+2523010 from *NuSTAR* observations using `borus02`.

Parameter	Fixing only $N_{\rm H,LOS}$	Fixing only $C_{\rm Ins}$	Varying both
$C_{\rm Ins,NuS1}$ [(a)]	$1.23^{+0.05}_{-0.04}$	$1.53^{+0.07}_{-0.07}$	$1.25^{+0.07}_{-0.05}$
$C_{\rm Ins,NuS2}$ [(b)]	$1.94^{+0.09}_{-0.09}$	"	$1.94^{+0.09}_{-0.09}$
$N_{\rm H,LOS,NuS1}$ [(c)]	*	$5.63^{+1.96}_{-1.78}$	$0.33^{+1.61}_{-*}$
$N_{\rm H,LOS,NuS2}$ [(d)]	"	*	*
χ^2/d.o.f.	558/587	645/587	558/586

Notes. [(a)]Cross-calibration value from FPMA detector, observed in 2017. [(b)]Cross-calibration value from FPMA detector, observed in 2020. [(c)]LOS column density from FPMA detector in 10^{22}cm^{-2}, observed in 2017. [(d)]LOS column density from FPMA detector in 2020 is unconstrained, represented as *.

regime, `borus02` fails to compute the covering factor and inclination angle properly. Noticing the absence of a reflection component, we also tested a simple phenomenological model using photoelectric absorption and a power law above 3 keV. We find $\chi^2_\nu \sim 0.99$ with $N_{\rm H,LOS}$ and Γ within the error range of `borus02` results, considering a direct power law along the LOS. Therefore, for the similarity of the results and to maintain consistency with the other sources, we have shown the results of physically motivated torus models only in Table A.5.

Furthermore, for this source, we also find a cross-calibration variability for different *NuSTAR* observations. Therefore, in Table 4 we show a comparative study of the *NuSTAR* observations of this source taken in May 2017 and April 2020, which was carried out in order to check for flux and LOS column density variability; the table is similar to Table 3. The cross-calibration value is measured with respect to the *XMM-Newton* observation of November 2017. Here, we also see the reduced χ^2 value does not show any significant change when fixing only LOS column density, but the χ^2/d.o.f. increases and worsens the fit when we fix the cross-calibration parameter only. Therefore, similarly to the previous case, the observed flux change for this source can also be explained by the intrinsic luminosity variability.

4.7. ESO138-G001

This source was marked as a CT-AGN based on the data of *XMM-Newton* and *Swift*-BAT, which suggest log $N_{\rm H} = 25.25^{+*}_{-0.31}$ cm^{-2}. For our analysis, we used *XMM-Newton* and *NuSTAR* observations, both having excellent count statistics ($\sim 45k$ counts in the 0.5−10 keV and $\sim 12.7k$ counts in the 3−50 keV band, respectively). The cross-calibration ratio of the *NuSTAR* detector on *XMM-Newton* for the source is ∼1.15.

The fit is worse (reduced $\chi^2 \sim 1.33-1.45$; see Table A.6 and Fig. B.6) than those measured for the other sources. The models are better fitted in the soft X-rays when adding all the emission lines listed in Table 5 following the previous works of Piconcelli et al. (2011), De Cicco et al. (2015). All three models are almost consistent with each other.

Studying all the models, the LOS column density $N_{\rm H,LOS} = (0.30-0.40)\times10^{24}$ cm^{-2} shows Compton-thin clouds, which differs from the results of Ricci et al. (2015). In comparison with the average column density of the torus, the decoupled `MYTorus` (Face-On) and `borus02` estimate $N_{\rm H,tor} = (2.45-10.43)\times 10^{24}$ cm^{-2}, supporting a CT average column density scenario. It

Table 5. Best-fitting parameters of the different emission lines on ESO138-G001, using different torus models.

Lines	MyTorus Edge-on	MyTorus Face-on	borus02
EW of Mg XI	$0.10^{+0.01}_{-0.01}$	$0.09^{+0.01}_{-0.01}$	$0.10^{+0.01}_{-0.01}$
Intensity of Mg XI 10^{-5}	$0.66^{+0.06}_{-0.06}$	$0.66^{+0.06}_{-0.06}$	$0.67^{+0.06}_{-0.06}$
EW of S XV	$0.10^{+0.02}_{-0.02}$	$0.10^{+0.02}_{-0.02}$	$0.09^{+0.02}_{-0.01}$
Intensity of S XV 10^{-5}	$0.23^{+0.05}_{-0.05}$	$0.23^{+0.05}_{-0.05}$	$0.22^{+0.05}_{-0.05}$
EW of Si XIII	$0.07^{+0.02}_{-0.01}$	$0.07^{+0.01}_{-0.01}$	$0.07^{+0.01}_{-0.01}$
Intensity of Si XIII 10^{-5}	$0.28^{+0.04}_{-0.04}$	$0.28^{+0.04}_{-0.04}$	$0.28^{+0.04}_{-0.04}$

Notes. We summarise here the details of the three most prominent emission lines in Fig. B.6 of joint *XMM-Newton–NuSTAR* spectra following the publications- De Cicco et al. (2015), Piconcelli et al. (2011). Equivalent width (EW) of the lines are shown in keV. Normalisation of line components are shown in photons/cm^{-2} s^{-1}.

is also noticeable that the `borus02` gives a comparatively better reduced χ^2 value (∼1.33) and $\Gamma \sim 1.95-1.99$. In addition, the `borus02` model further computes a moderate-to-high covering factor (0.68−0.83), but low inclination angle with unconstrained error. We also had to include an extra Gaussian line profile for the fluorescent lines in the models to account for a broader line profile than the one implemented within the torus models. The high $N_{\rm H,tor}$ and high covering factor show that the reprocessed emission is significantly dominant with a prominent Fe line. In `borus02`, adding the Gaussian line improves the fit significantly, with an F-statistic value ≈42.2.

5. Discussion

This paper reports the analysis of seven CT-AGN candidates: MCG-02-12-017, NGC 2788A, NGC 4180, 2MASX J20145928+2523010, ESO406 G-004, NGC 1106, and ESO138 G-001 from the 100 month Palermo BAT sample. For the first time, we analysed the *NuSTAR* spectra of these sources using `MYTorus` and `borus02`.

5.1. Clumpy torus and variability

The LOS column density and average torus column density of three out of the seven sources in our sample (NGC 4180, NGC 2788A and NGC 1106) are found to be in agreement within their uncertainty ranges and above the Compton-thick threshold ($>10^{24}$ cm^{-2}). For ESO406 G-004, the column densities are compatible within their error range, but fall in the Compton-thin range. The remaining three sources (MCG-02-12-017, 2MASX J20145928+2523010, ESO138 G-001) show incompatible column densities, hinting at a clumpy nature of the obscuring medium. In the left panel of Fig. 2, we compare the LOS column density results of our sample using `borus02` along with the results of Ricci et al. (2015). All seven candidates from Ricci et al. (2015) lie above the CT threshold with large uncertainties, whereas the use of *NuSTAR* data instead of *Swift*-BAT reduces the error bar significantly, displaying only three sources above the CT line, leading to the confirmation of only three sources as CT. The right panel of Fig. 2 shows a clear trend of the flux ratio at 2–10 keV as a function of $N_{\rm H,LOS}$: the larger the LOS column density, the stronger the flux of reflected continuum over direct continuum.

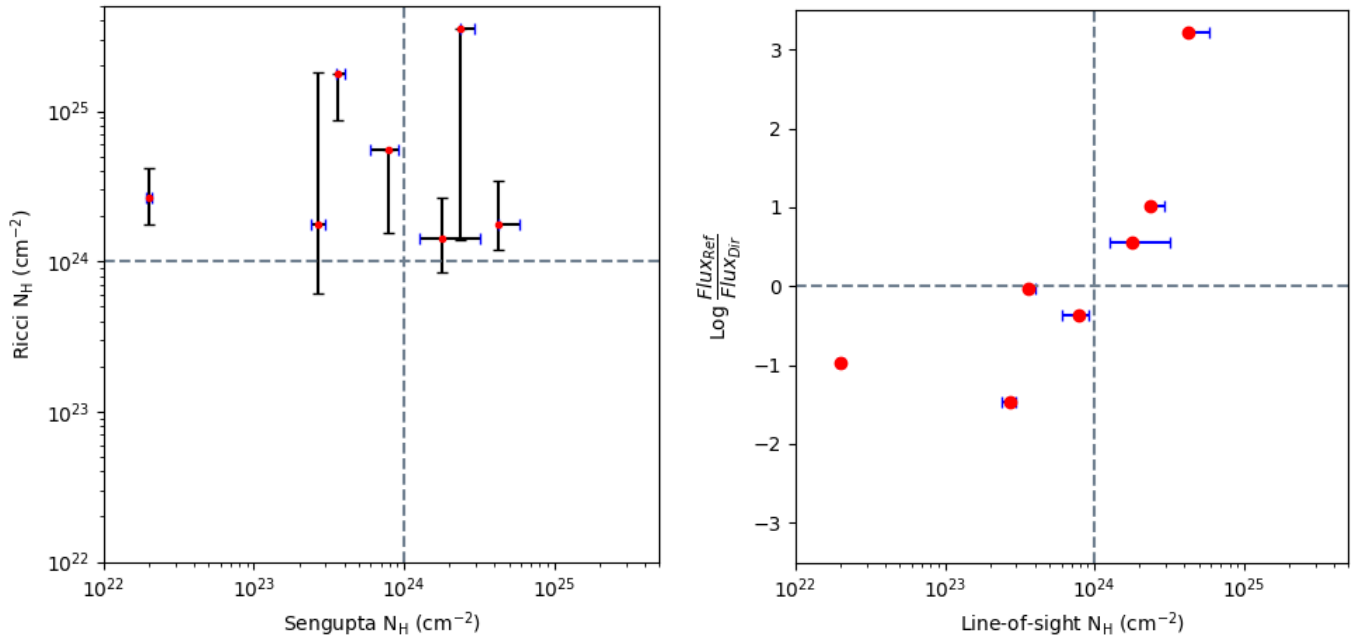

Fig. 2. Comparisons of X-ray spectral properties of the seven sources. *Left:* comparison of the LOS column density values (as red dot) and its uncertainty values from Ricci et al. (2015) (black markers) with those of the present study (blue markers). The horizontal and vertical grey-dashed lines classify the CT column density threshold. *Right*: observed (i.e. non-absorption corrected) flux ratio of the reflected component over the direct transmitted component in the 2–10 keV band for each source of our sample, plotted along the LOS column density on the *X*-axis.

Furthermore, in Fig. 3, we show the distribution of $N_{\rm H,LOS}$ and $N_{\rm H,avr}$ of our sample AGN along with all the previous results of the CT-AGN candidates analysed by the Clemson-INAF group. The $\frac{N_{\rm H,LOS}}{N_{\rm H,avr}} = 1$ line is shown as a brown-dashed line and 1:2 and 2:1 ratios are shown as pink dot-dashed lines to classify the sources with a comparatively homogeneous torus when they produce a column density ratio of within ∼0.5−2.0. Only 12 sources (∼22% of the sample) fall within this region. The remaining 43 sources (∼78% of the sample) instead show significant inhomogeneity, and considering the error bar at the 3σ level, 34 sources (∼62%) fall completely outside the given area. This is also a natural outcome of the CCA scenario, in which the multi-phase clouds continuously rain through the meso scale, thus recurrently obscuring the LOS. The residual gas experiencing less inelastic collisions (and therefore less angular momentum cancellation) tends to accumulate in a clumpy torus-like structure at this scale (Gaspari et al. 2017). Therefore, based on all previous results, in addition to those presented in this work, we can conclude that most of these obscured active galaxies have a significantly clumpy torus (∼78% of the total population). It is also important to note that the two column densities are significantly uncorrelated. By statistically analysing the parameters for all 55 sources, their Pearson correlation coefficient[5] yields $\rho \approx 0.003$ (similar to the value of −0.017 obtained by Torres-Albà et al. 2021). This suggests that a bona fide CT-AGN is not necessarily likely to be made of CT-torus. As supported by hydrodynamical simulations (see e.g., Gaspari et al. 2020), a realistic torus is a composition of multi-phase and multi-scale clouds, whose integral (e.g., density) can substantially change along each LOS. The non-correlation we find is even consistent with the results of Zhao et al. (2021), in which a sample of approximately 100 local Compton-thin AGN were studied (along with CT-AGN) using high-quality *NuSTAR* data along with soft X-ray data, with the authors showing that similar values of $N_{\rm H,tor}$ (∼1.4×10^{24} cm^{-2}) are found for different $N_{\rm H,LOS}$. In Fig. 3, we increased our sample by including 74 sources from Zhao et al. (2021), marked as small grey circles. All of these sources have $N_{\rm H,LOS} > 10^{22}$ cm^{-2}. We find that the total percentage of homogeneous tori comes down to ∼16% of the enlarged sample, including the Compton-thin sources. By calculating the Pearson correlation coefficient between the column densities with this enlarged sample, we find a similar non-correlation scenario (∼−0.012), as obtained before including these Compton-thin AGN.

Through multi-epoch X-ray monitoring of these obscured sources, we can study the LOS column density variability and confirm the inhomogeneity of the circumnuclear cloud distribution. Some previous observations have reported extreme variability, and even a 'changing-look' nature from CT to Compton-thin or vice versa; for example, for NGC 7582 (Bianchi et al. 2009; Rivers et al. 2015), IC 751 (Ricci et al. 2016), and NGC 1358 (Marchesi et al. 2022), among others. In our sample, 2MASX J20145928+2523010 shows strong variability over a three-year time span. On the other hand, ESO138 G-001 shows almost no variability after a seven-year observational gap (Sect. 4.7). In order to obtain a clearer picture of the variability of such sources (i.e. clumpiness) over timescales from weeks to years, we would need follow-up observations with longer exposures on each source. Nevertheless, to properly assess the complex cloud distribution within the torus of each of these obscured sources, a joint analysis of both X-ray and mid-infrared (MIR) is required at multiple epochs (Berta et al. 2013; Buchner et al. 2019; Esparza-Arredondo et al. 2021). We will consider this in future work.

5.2. Updated census of local CT-AGN candidates

Out of the seven 100 month BAT candidate CT-AGN analysed in this work, we confirm three bona fide CT-AGN. This brings the total number of CT-AGN at $z < 0.05$ to 35[6]

[5] $\rho \approx 1$ or $\rho \approx -1$ for strong linear correlation or anti-correlation, respectively, and $\rho \approx 0$ for lack of correlation.

[6] https://science.clemson.edu/ctagn/

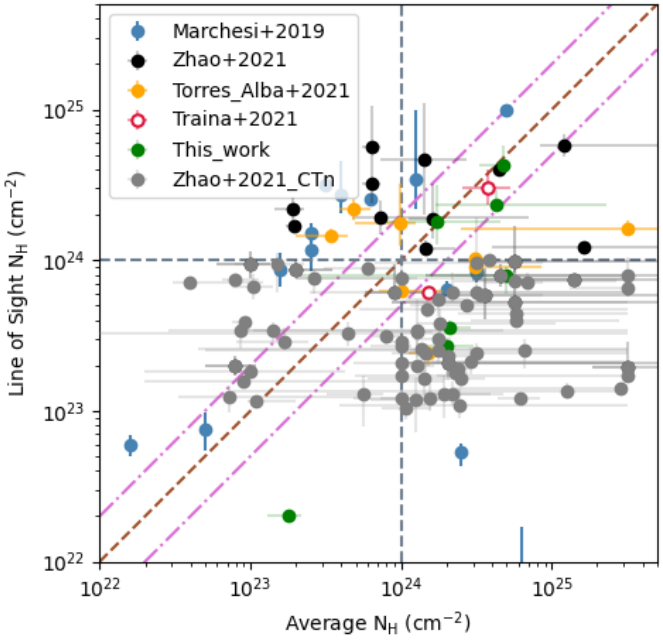

Fig. 3. Census of the previous results of CT-AGN candidates (selected from Ricci et al. 2015) having $z < 0.01$ with archival *NuSTAR* data, analysed by the Clemson-INAF group: Marchesi et al. (2018), Zhao et al. (2021), Torres-Albà et al. (2021), Traina et al. (2021) and including our analysis. The sample of these CT-AGN candidates are marked as large circles. In the parameter space of average vs LOS column density, grey-dashed lines drawn horizontally and vertically marks the CT column density threshold. The brown-dashed diagonal line (i.e the "Line of Homogeneity") identifies an homogeneous obscuring material distribution. The region within the pink dot-dashed lines is used to classify the number of sources with homogeneous torus. We also included the sample of 74 Compton-Thin sources from Zhao et al. (2021), shown as small grey circles.

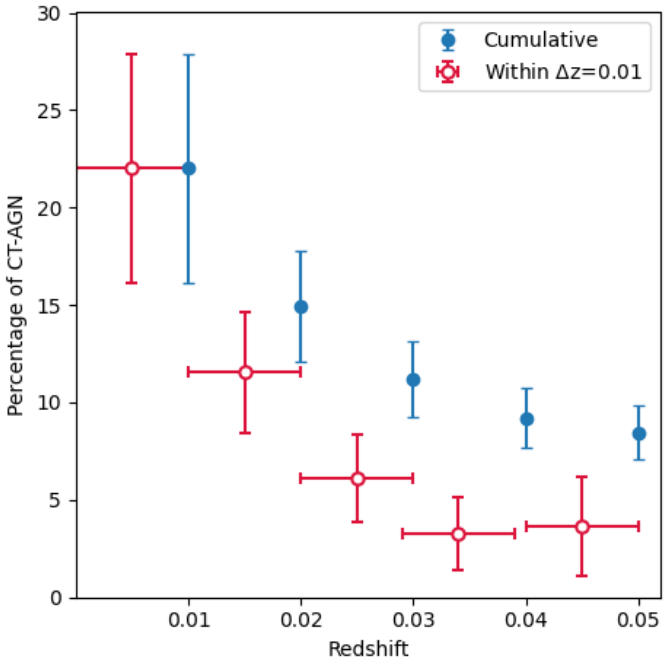

Fig. 4. Evolution of observed CT-AGN fraction from the 100 month *Swift*-BAT catalogue as a function of redshift (for $z < 0.05$). The red points represent the CT-AGN fraction within the given redshift bin of 0.01 and blue points show the cumulative value of the fraction within the given redshift. The displayed error bars are in binomial statistics. This figure is updated from the CT-AGN fraction plot of Torres-Albà et al. (2021).

(Koss et al. 2016; Oda et al. 2017; Marchesi et al. 2018, 2019a,b; Georgantopoulos & Akylas 2019; Tanimoto et al. 2019; Kammoun et al. 2020; Zhao et al. 2021, 2020; Traina et al. 2021; Torres-Albà et al. 2021). In the left panel of Fig. 3, we study 55 CT-AGN candidates analysed by our Clemson-INAF group in the parameter space of observed $N_{H,LOS}$ and computed $N_{H,avr}$. Of these, 27 (~50%) have $N_{H,LOS} > 10^{24}$ cm^{-2}.

The total percentage of confirmed CT-AGN from *Swift*-BAT selection within the local Universe ($z < 0.05$) is ~8% (35/414), which is much lower than the CT-AGN fraction predicted by the population synthesis models. Our results also update the CT-AGN fraction within the distance $z < 0.01$ to (~22% ± 5.9)%[7] (11 CT-AGN out of 50 AGN; Torres-Albà et al. 2021 showed 10 CT-AGN). Figure 4 shows the fraction of CT-AGN from the total AGN population in the 100 month *Swift*-BAT catalogue. The fraction drops when moving towards higher redshifts ($z > 0.01$) because the CT-AGN sources become too faint to be detected by *Swift*-BAT (Koss et al. 2016).

5.3. Comparison with XClumpy results

Recently, Tanimoto et al. 2022 (T22 hereafter) published the results of an X-ray spectral analysis with the *'XClumpy'* model (Tanimoto et al. 2019) of the sources analysed in this work (as part of a larger sample of low-redshift, heavily obscured AGN).

[7] Standard error in binomial distribution.

The *XClumpy* model considers the torus as clumpy and inhomogeneous, assuming a power-law distribution along the radial axis and a Gaussian distribution along the vertical axis of the torus. Below, we compare the results of these latter authors with those obtained using `MYTorus` decoupled and `borus02` in this work.

- MCG-02-12-017: For this source, T22 used the quasi-simultaneous observations of *XMM-Newton* and *NuSTAR* (ObsID: 60101015002). The LOS column density and photon index, at 90% confidence, are $N_{H,LOS} = (0.21-0.28) \times 10^{24}$ cm^{-2} and $\Gamma = 1.53-1.88$, respectively. The results are very consistent with ours (see Table 2). Similarly, the computed equatorial (average) column density mostly falls within the limits of the error range ($N_{H,eq} = (1.16-9.59) \times 10^{24}$ cm^{-2}) of our analysis, which is also in agreement with our prediction of the clumpy nature of the torus. Overall, for this source, the *XClumpy* model is in agreement with the decoupled `MYTorus` and `borus02` models.
- NGC 4180: For this source, T22 used the observations of *Chandra* and *NuSTAR* (ObsID: 60201038002). The LOS column density and photon index, at the 90% confidence level, are $N_{H,LOS} = (0.68-3.75) \times 10^{24}$ cm^{-2} and $\Gamma = 1.44-1.66$, respectively. The results are consistent with the decoupled Face-ON `MYTorus` and `borus02` results (see Table A.1). Similarly, the computed equatorial (average) column density mostly falls within the range ($N_{H,eq} = (1.92-4.10) \times 10^{24}$ cm^{-2}) computed in our analysis, which is also in agreement with our prediction of the clumpy nature of the torus. Even though we only used *NuSTAR* data on this source in our analysis, the results of the `MYTorus` and `borus02` model are still in agreement with the *XClumpy* results.
- NGC 2788A: For this source, T22 used the observations of *Suzaku* (obsID: 710007010) and *NuSTAR*

Table 6. Comparisons of best-fit values for Γ (photon index) and torus column density using the torus models.

Models:	`borus02`		`MYTorus`	(Decoupled edge-on)	*XClumpy*	(from T22)
Sources	Γ	$N_{\rm H,torus}$ (10^{24} cm^{-2})	Γ	$N_{\rm H,S}$ (10^{24} cm^{-2})	Γ	$N_{\rm H,eq}$ (10^{24} cm^{-2})
MCG-02-12-017	$2.11^{+0.13}_{-0.16}$	$1.98^{+1.07}_{-0.52}$	$1.94^{+0.14}_{-0.14}$	$2.00^{+2.83}_{-1.10}$	$1.54^{+0.18}_{-0.45}$	$9.59^{+*}_{-8.43}$
NGC4180	$1.55^{+0.44}_{-*}$	$1.74^{+2.82}_{-1.08}$	$1.66^{+0.39}_{-*}$	$1.97^{+0.33}_{-0.73}$	$1.61^{+0.05}_{-0.17}$	$4.10^{+*}_{-2.18}$
NGC2788A	$1.95^{+0.32}_{-0.31}$	$4.26^{+18.43}_{-2.54}$	$1.56^{+0.20}_{-*}$	$1.25^{+0.24}_{-0.60}$	$1.67^{+0.11}_{-0.08}$	$2.37^{+2.20}_{-0.19}$
NGC1106	$1.92^{+0.44}_{-0.35}$	$4.83^{+*}_{-1.38}$	$1.40^{+0.00}_{-*}$	$1.46^{+0.18}_{-0.12}$	$1.67^{+0.16}_{-0.30}$	$8.17^{+1.63}_{-1.51}$
ESO406-G004	$1.42^{+0.02}_{-*}$	$4.97^{+*}_{-4.80}$	$1.48^{+0.30}_{-*}$	$0.49^{+1.11}_{-0.62}$	$1.10^{+0.28}_{-*}$	$0.64^{+0.55}_{-0.23}$
2MASX J20145928+2523010	$1.52^{+0.05}_{-0.04}$	$0.18^{+0.05}_{-0.04}$	$1.79^{+0.10}_{-0.10}$	$0.12^{+0.04}_{-0.03}$	$1.42^{+0.03}_{-0.09}$	$1.01^{+0.89}_{-0.67}$
ESO138-G001	$1.98^{+0.01}_{-0.03}$	$10.35^{+0.08}_{-0.08}$	$1.53^{+0.05}_{-0.05}$	$1.47^{+0.60}_{-0.49}$	$1.45^{+0.03}_{-0.06}$	$5.34^{+1.53}_{-3.66}$

(ObsID: 60469001002). The LOS column density and photon index, at the 90% confidence level, are $N_{\rm H,LOS}$ = (1.55−2.83) × 10^{24} cm^{-2} and Γ = 1.59−1.78, respectively. The results are very consistent with our results (see Table A.2), even though we used *Swift*-XRT instead of *Suzaku* at energies E < 10 keV. The computed equatorial (average) column density also falls within the range ($N_{\rm H,eq}$ = (2.18−4.57)×10^{24} cm^{-2}) of our analysis. Even for the covering factor measurement, *XClumpy* estimates $\theta_{\rm Tor}$ = 19°−46°, which significantly narrows the error range and falls within the `borus02` computed range of $\theta_{\rm Tor}$ = 16°−78°. Also, while computing the inclination angle $\theta_{\rm Inc}$ = 62°−85°, the values can be considered to be in agreement within the uncertainties with the `borus02` fitting (47°−72°). Overall, for this source, the results obtained using the *XClumpy* model can be regarded as consistent with those obtained using the decoupled `MYTorus` and `borus02` ones.

– NGC 1106: For this source, T22 used the observations of *XMM-Newton* and *NuSTAR* (ObsID: 60469002002). The LOS column density and photon index, at 90% confidence, are found to be $N_{\rm H,LOS}$ = 3.45−4.29 × 10^{24} cm^{-2} and Γ = 1.37−1.83, respectively. These results are consistent with our results (see Table A.3). On the other hand, the computed equatorial (average) column density falls in the upper limits of the error range ($N_{\rm H,eq}$ = (6.66−9.80) × 10^{24} cm^{-2}) compared to our analysis. Regarding the computation of the inclination angle $\theta_{\rm Inc}$ = 60°−77° and covering factor $\theta_{\rm Tor}$ = 14°−31°, the results of T22 fall within the large confidence range of our analysis ($\theta_{\rm Inc}$ = 28°−74° and $\theta_{\rm Tor}$ = 11°−51°). It is noticeable that the error ranges are significantly reduced while using *XClumpy*. Nevertheless, for this source, the *XClumpy* model results are compatible with those obtained using the decoupled `MYTorus` and `borus02` models.

– ESO406 G-004: For this source, T22 used the observations of *Swift*-XRT (ObsID: 00081420001) and *NuSTAR* (ObsID: 60161799002). The LOS column density and photon index, at the 90% confidence level, are found to be $N_{\rm H,LOS}$ = (0.38−6.34) × 10^{24} cm^{-2} and Γ = 1.10−1.38, respectively. As we used *Chandra* and both available *NuSTAR* data, our results show better constraints (see Table A.4) on this source compared to the results of T22. However, the computed equatorial (average) column density mostly falls within the range ($N_{\rm H,eq}$ = (0.41−1.19)×10^{24} cm^{-2}) of our analysis. The *XClumpy* model is compatible with decoupled `MYTorus` and `borus02` results.

– 2MASX J20145928+2523010: For this source, T22 used the observations of *XMM-Newton* and *NuSTAR* (ObsID: 60201032002). For the LOS column density and photon index, at 90% confidence, T22 find $N_{\rm H,LOS}$ = (0.01−0.03) × 10^{24} cm^{-2} and Γ = 1.33−1.45, respectively. The results of $N_{\rm H,LOS}$ show consistency with our results, but the Γ value is much lower than provided by `MYTorus` and `borus02` (see Table A.5). However, the computed equatorial (average) column density falls within the range ($N_{\rm H,eq}$ = (0.34−1.90) × 10^{24} cm^{-2}) of our analysis, which is also in agreement with our prediction of clumpy torus clouds. Overall, for this source, the *XClumpy* model is consistent with most of the results of decoupled `MYTorus` and `borus02` models, except in Γ.

– ESO138 G-001: For this source, T22 used the observations of *XMM-Newton* and *NuSTAR* (ObsID: 60201040002). T22 find an LOS column density and photon index, at 90% confidence, of $N_{\rm H,LOS}$ = (0.42−0.50) × 10^{24} cm^{-2} and Γ = 1.42−1.51, respectively. The results are quite inconsistent with our results (see Table A.6), especially when compared to the photon index from `borus02`, which is Γ = 1.95−1.99 . Similarly, the computed equatorial (average) column density has a value within the range ($N_{\rm H,eq}$ = (1.68−6.87)×10^{24} cm^{-2}) of our analysis. Their covering factor of $\theta_{\rm Tor}$ = 10°−13° lies far below the `borus02` estimates of $\theta_{\rm Tor}$ = 34°−47°. For this source, the *XClumpy* model in T22 is inconsistent with the decoupled `MYTorus` and `borus02` results. We note that `borus02` results in a better fit (reduced χ^2 value ∼1.32) compared to the fit found by T22 (reduced χ^2 = 1.39).

In summary, from the above comparisons, we find *XClumpy* places stronger constraints on the different torus parameters with respect to `borus02` and `MYTorus` given the smaller associated uncertainties. The only exception is ESO138 G-001, which is best-fitted using `borus02` in our analysis, because T22 did not include the prominent emission lines that we mention in Table 5. We also notice that the *XClumpy* model shifts the best-fit value of photon index to harder values by ∼6%−22% compared to `borus02` and by ∼0.6%−26% compared to the best-fit model of decoupled `MYTorus` in our sample. In Table 6, we show the values of photon index and average torus column density computed using different torus models for each source. We note that T22 used only one *NuSTAR* observation for each source. In this work, we used all the available observations from *NuSTAR* for these heavily obscured sources in order to increase the photon statistic over 10keV and minimise the under- and overestimation of spectral parameters. Overall, for our sources, we do not find

Table 7. Best-fit `borus02` parameters for the sample.

Sources	Γ	$N_{\rm H,LOS}$ (10^{24} cm^{-2})	$N_{\rm H,torus}$ (10^{24} cm^{-2})	$C_{\rm Tor}$	$\theta_{\rm Inc}$ (Degees)
MCG-02-12-017	$2.11^{+0.13}_{-0.16}$	$0.27^{+0.03}_{-0.03}$	$1.98^{+1.07}_{-0.52}$	$1.00^{+*}_{-0.35}$	49^{+*}_{-*}
NGC4180	$1.55^{+0.44}_{-*}$	$1.78^{+1.40}_{-0.51}$	$1.74^{+2.82}_{-1.08}$	$0.88^{+*}_{-0.77}$	49^{+12}_{-*}
NGC2788A	$1.95^{+0.32}_{-0.31}$	$2.34^{+*}_{-0.58}$	$4.26^{+18.43}_{-2.54}$	$0.49^{+0.47}_{-0.28}$	63^{+9}_{-16}
NGC1106	$1.92^{+0.44}_{-0.35}$	$4.79^{+*}_{-1.96}$	$4.83^{+*}_{-1.38}$	$0.87^{+0.11}_{-0.24}$	37^{+37}_{-9}
ESO406-G004	$1.42^{+0.02}_{-*}$	$0.79^{+0.04}_{-0.12}$	$4.97^{+*}_{-4.80}$	0.10^{+*}_{-*}	18^{+69}_{-*}
2MASX J20145928+2523010	$1.52^{+0.05}_{-0.04}$	$0.02^{+0.00}_{-0.00}$	$0.18^{+0.04}_{-0.05}$	$1.00^{+*}_{-0.23}$	18^{+*}_{-*}
ESO138-G001	$1.98^{+0.01}_{-0.03}$	$0.47^{+0.07}_{-0.06}$	$10.35^{+0.08}_{-0.08}$	$0.80^{+0.03}_{-0.12}$	18^{+*}_{-*}

any significant discrepancies when using *XClumpy* in comparison with `borus02` and decoupled `MYTorus` models.

6. Conclusions and summary

In this work, we studied and classified seven CT-AGN candidates from the 100 month *Swift*-BAT catalogue using archival *NuSTAR* observations. All sources have at least one *NuSTAR* observation covering the 3–50 keV energy range. In the 0.6–10 keV band, we used *XMM-Newton* data for three targets, *Chandra* data for two targets, and both *XMM-Newton* and *Chandra* for one target. NGC 2788A has only *Swift*-XRT data in the soft X-ray. We classified the sources on the basis of their best-fit value of LOS hydrogen column density; that is, if $N_{\rm H,LOS} \geq 10^{24}$ cm^{-2} the candidates are marked as bona fide CT-AGN. Otherwise, they are identified as partially CT-AGN or Compton-thin AGN depending on their column density. The summary of our results and conclusions are as follows:

1. From the seven CT-AGN candidates, three are confirmed CT-AGN with moderate to high covering factors based on *NuSTAR* data above 10 keV. Three of them show a Compton-thin LOS column density, but a torus column density above the CT threshold. Only 2MASX J20145928+2523010 shows Compton-thin values in both the column densities. A summary of the results for all of these sources with the `borus02` model is displayed in Table 7.
2. This present work updates the total number of *NuSTAR*-confirmed CT-AGN to 35 for $z < 0.05$, which is ∼8% of the total AGN population in the 100 month BAT catalogue. This value is still relatively far below the value predicted by the CXB population synthesis models (∼20%−50%), which suggests that a significant fraction of heavily obscured AGN are missed even by a hard-X-ray telescope such as *Swift*-BAT.
3. Out of 55 CT-AGN candidates analysed by our Clemson-INAF research group, adding the results of this work brings the population of confirmed CT-AGN to 27 (∼50%). Among these, only 14 (∼25%) candidates show both $N_{\rm H,LOS}$ and $N_{\rm H,avr}$ above the CT threshold.
4. We find no correlation between these two column densities ($N_{\rm H,LOS}$ and $N_{\rm H,avr}$) from our sample. Our results state that identifying a bona fide CT-AGN, that is, an obscured AGN with $N_{\rm H,LOS} > 10^{24}$ cm^{-2} , does not necessarily mean that the torus is also CT. Similarly, a Compton-thin $N_{\rm H,LOS}$ does not necessarily signify that the torus is also Compton-thin.
5. Most of these obscured galaxies have a significantly clumpy or inhomogeneous distribution of clouds. Multi-epoch monitoring of these sources using telescopes such as *XMM-Newton*, *Chandra*, and *NuSTAR* will help us to study their intrinsic flux and LOS column density variability. This will lead to a better understanding of cloud movements in the obscuring medium and X-ray emission from the central engine.
6. `MYTorus` and `borus02` results are consistent with each other in estimating the column densities and other parameters of the sources. In most cases, `borus02` shows better fitting from a statistical point of view. It also estimates the torus opening angle and inclination angle of the obscured AGN, which are fixed parameters in `MYTorus`.
7. We find our results on the seven CT-AGN candidates using the uniform torus models to be compatible with the results of the non-uniform torus model *XClumpy* in Tanimoto et al. (2022). However, we also notice the trend that *XClumpy* shifts the photon index to harder values in comparison to the uniform torus models we use here. For reference, we display the Γ and torus column density values of T22 with respect to our results in Table 6.

For future works, a joint analysis of the X-ray properties and the reprocessed emission at mid-IR will be carried out in order to gain a better understanding of the torus structure and obscuration properties (Sengupta et al., in prep.). In future studies, we will also use multi-epoch observations of some of these sources in the framework of theoretical models, such as CCA (Gaspari et al. 2013), warped-accretion disk (Buchner et al. 2021), and others (Torres-Albà et al. 2023; Sengupta et al., in prep.; Pizzetti et al., in prep.).

Acknowledgements. We thank the referee for the useful suggestions that helped us in improving the paper. This research has made use of the *NuSTAR* Data Analysis Software (NuSTARDAS) jointly developed by the ASI Space Science Data Center (SSDC, Italy) and the California Institute of Technology (Caltech, USA). DS acknowledges the PhD and "MARCO POLO UNIVERSITY PROGRAM" funding from the Dipartimento di Fisica e Astronomia (DIFA), Universitá di Bologna. DS and SM acknowledge the funding from INAF "Progetti di Ricerca di Rilevante Interesse Nazionale" (PRIN), Bando 2019 (project: "Piercing through the clouds: a multiwavelength study of obscured accretion in nearby supermassive black holes"). MG acknowledges partial support by HST GO-15890.020/023-A and the BlackHoleWeather program.

References

Ajello, Jr., G., Sato, G., Willis, D. R., et al. 2008, ApJ, 689, 666
Ananna, T. T., Treister, E., Urry, C. M., et al. 2019, ApJ, 871, 240
Anders, E., & Grevesse, N. 1989, Geochim. Cosmochim. Acta, 53, 197
Arnaud, K. A. 1996, in Astronomical Data Analysis Software and Systems V, eds. G. H. Jacoby, & J. Barnes, ASP Conf. Ser., 101, 17
Baloković, M., Brightman, M., Harrison, F. A., et al. 2018, ApJ, 854, 42
Bennett, C. L., Larson, D., Weiland, J. L., & Hinshaw, G. 2014, ApJ, 794, 135
Berta, S., Lutz, D., Santini, P., et al. 2013, A&A, 551, A100
Bianchi, S., Piconcelli, E., Chiaberge, M., et al. 2009, ApJ, 695, 781

Brightman, M., & Nandra, K. 2011, MNRAS, 413, 1206
Buchner, J., Brightman, M., Nandra, K., Nikutta, R., & Bauer, F. E. 2019, A&A, 629, A16
Buchner, J., Brightman, M., Baloković, M., et al. 2021, A&A, 651, A58
Comastri 2004, Supermassive Black Holes in the Distant Universe (Springer), 245
De Cicco, M., Marinucci, A., Bianchi, S., et al. 2015, MNRAS, 453, 2155
Esparza-Arredondo, D., Gonzalez-Martín, O., Dultzin, D., et al. 2021, A&A, 651, A91
Gaspari, M., Ruszkowski, M., & Oh, S. P. 2013, MNRAS, 432, 3401
Gaspari, M., Temi, P., & Brighenti, F. 2017, MNRAS, 466, 677
Gaspari, M., Eckert, D., Ettori, S., et al. 2019, ApJ, 884, 169
Gaspari, M., Tombesi, F., & Cappi, M. 2020, Nat. Astron., 4, 10
Georgantopoulos, I., & Akylas, A. 2019, A&A, 621, A28
Gilli, R., Comastri, A., & Hasinger, G. 2007, A&A, 463, 79
Gilli, R., Norman, C., Calura, F., et al. 2022, A&A, 666, A17
Harrison, F. A., Craig, W. W., Christensen, F. E., et al. 2013, ApJ, 770, 103
Hickox, R. C., & Markevitch, M. 2006, ApJ, 645, 95
Kaastra, J. 1992, Internal SRON-Leiden Report
Kalberla, P. M. W., Burton, W. B., Hartmann, D., et al. 2005, A&A, 440, 775
Kammoun, E. S., Miller, J. M., Koss, M., et al. 2020, ApJ, 901, 161
Koss, M. J., Assef, R., Baloković, M., et al. 2016, ApJ, 825, 85
Liedahl, D. A., Osterheld, A. L., & Goldstein, W. H. 1995, ApJ, 438, L115
Maccagni, F. M., Serra, P., Gaspari, M., et al. 2021, A&A, 656, A45
Marchesi, S., Lanzuisi, G., Civano, F., et al. 2016, ApJ, 830, 100
Marchesi, S., Ajello, M., Marcotulli, L., et al. 2018, ApJ, 854, 49
Marchesi, S., Ajello, M., Zhao, X., et al. 2019a, ApJ, 882, 162
Marchesi, S., Ajello, M., Zhao, X., et al. 2019b, ApJ, 872, 8
Marchesi, S., Zhao, X., Torres-Albà, N., et al. 2022, ApJ, 935, 114
McKinley, B., Tingay, S. J., Gaspari, M., et al. 2022, Nat. Astron., 6, 109
Mewe, R., Gronenschild, E., & Van Den Oord, G. 1985, A&AS, 62, 197
Murphy, K. D., & Yaqoob, T. 2009, MNRAS, 397, 1549
Oda, S., Tanimoto, A., Ueda, Y., et al. 2017, ApJ, 835, 179
Oh, K., Koss, M., Markwardt, C. B., et al. 2018, ApJS, 235, 4
Piconcelli, E., Bianchi, S., Vignali, C., Jiménez-Bailón, E., & Fiore, F. 2011, A&A, 534, A126
Pizzetti, A., Torres-Albà, N., Marchesi, S., et al. 2022, ApJ, 936, 149
Ricci, C., Ueda, Y., Koss, M. J., et al. 2015, ApJ, 815, L13
Ricci, C., Bauer, F. E., Treister, E., et al. 2016, ApJ, 819, 4
Rivers, E., Baloković, M., Arévalo, P., et al. 2015, ApJ, 815, 55
Rose, T., Edge, A. C., Combes, F., et al. 2019, MNRAS, 489, 349
Silver, R., Torres-Albà, N., Zhao, X., et al. 2022, ApJ, 940, 148
Tanimoto, A., Ueda, Y., Odaka, H., et al. 2019, ApJ, 877, 95
Tanimoto, A., Ueda, Y., Odaka, H., Yamada, S., & Ricci, C. 2022, ApJS, 260, 30
Temi, P., Gaspari, M., Brighenti, F., et al. 2022, ApJ, 928, 150
Torres-Albà, N., Marchesi, S., Zhao, X., et al. 2021, ApJ, 922, 252
Torres-Albà, N., Marchesi, S., Zhao, X., et al. 2023, A&A, submitted [arXiv:2301.07138]
Traina, A., Marchesi, S., Vignali, C., et al. 2021, ApJ, 922, 159
Ueda, Y., Akiyama, M., Hasinger, G., Miyaji, T., & Watson, M. G. 2014, ApJ, 786, 104
Vasudevan, R. V., Mushotzky, R. F., & Gandhi, P. 2013, ApJ, 770, L37
Verner, D. A., Ferland, G. J., Korista, K. T., & Yakovlev, D. G. 1996, ApJ, 465, 487
Worsley, M., Fabian, A., Bauer, F., et al. 2005, MNRAS, 357, 1281
Yaqoob, T. 2012, MNRAS, 423, 3360
Zhao, X., Marchesi, S., & Ajello, M. 2019a, ApJ, 871, 182
Zhao, X., Marchesi, S., Ajello, M., et al. 2019b, ApJ, 870, 60
Zhao, X., Marchesi, S., Ajello, M., Baloković, M., & Fischer, T. 2020, ApJ, 894, 71
Zhao, X., Marchesi, S., Ajello, M., et al. 2021, A&A, 650, A57

Appendix A: Tables of X-Ray spectra

Table A.1. Summary of best-fit solutions of NuSTAR data using different models for NGC 4180

Model	MyTorus Edge-on	MyTorus Face-on	borus02
χ^2/dof	76/64	84/64	76/62
$C_{Ins}{}^a$	$1.47^{+0.27}_{-0.21}$	$1.48^{+0.26}_{-0.22}$	$1.47^{+0.26}_{-0.21}$
Γ	$1.66^{+0.39}_{-*}$	$1.40^{+0.22}_{-*}$	$1.55^{+0.44}_{-*}$
C_{Tor}	—	—	$0.88^{+*}_{-0.77}$
$\theta_{\rm Inc}$	—	—	49^{+12}_{-*}
$N_{H,z}$	$6.10^{+*}_{-4.30}$	$1.49^{+0.36}_{-0.24}$	$1.78^{+1.40}_{-0.51}$
$N_{H,S}$	$1.97^{+0.33}_{-0.73}$	$3.98^{+1.08}_{-*}$	$1.74^{+2.82}_{-1.08}$
$f_s 10^{-2}$	$0.40^{+1.02}_{-0.20}$	$0.55^{+1.05}_{-*}$	$2.27^{+1.31}_{-1.68}$
$F_{2-10keV}$	$1.34^{+0.22}_{-*}$	$1.30^{+0.15}_{-*}$	$1.33^{+3.82}_{-*}$
$F_{10-50keV}$	$4.49^{+20.85}_{-*}$	$4.73^{+9.22}_{-*}$	$4.54^{+0.39}_{-*}$
$L_{2-10keV}{}^b$	$11.01^{+51.43}_{-*}$	$2.72^{+3.18}_{-0.47}$	$3.21^{+7.78}_{-1.38}$
$L_{10-50keV}{}^c$	$19.05^{+89.05}_{-*}$	$7.14^{+0.38}_{-4.27}$	$6.63^{+15.99}_{-2.85}$

Notes. We summarise here the best-fits of *NuSTAR* spectra using different torus models between 3 and 50 keV, referred in Section 4.2. The statistics and degrees of freedom for each fit are also reported. The parameters are reported as in Table 2 if not mentioned otherwise. $^a C_{Ins}$ is the ratio of cross-normalisation constant between two *NuSTAR* observations through their FPMA detectors. ^{b}Intrinsic luminosity between 2 and 10 keV in 10^{41} erg s^{-1}. ^{c}Intrinsic luminosity between 10 and 50 keV in 10^{41} erg s^{-1}.

Table A.2. Summary of best-fit solutions of *Swift*-XRT and NuSTAR data using different models for NGC 2788A

Model	MyTorus Edge-on	MyTorus Face-on	borus02
C-Stat/dof	136/153	116/153	116/151
$C_{Ins_1}{}^a$	$1.12^{+0.58}_{-0.38}$	$0.93^{+0.40}_{-0.26}$	$0.94^{+0.40}_{-0.27}$
$C_{Ins_2}{}^b$	$1.36^{+0.70}_{-0.46}$	$1.13^{+0.48}_{-0.31}$	$1.14^{+0.47}_{-0.32}$
Γ	$1.56^{+0.20}_{-*}$	$1.75^{+0.17}_{-0.24}$	$1.95^{+0.32}_{-0.31}$
C_{Tor}	—	—	$0.49^{+0.47}_{-0.28}$
$\theta_{\rm Inc}$	—	—	63^{+9}_{-16}
$N_{H,z}$	$3.95^{+*}_{-1.91}$	$1.95^{+0.41}_{-0.28}$	$2.34^{+*}_{-0.58}$
$N_{H,S}$	$1.25^{+0.24}_{-0.60}$	$3.74^{+3.74}_{-1.37}$	$4.26^{+18.43}_{-2.54}$
f_s 10^{-2}	$0.23^{+0.26}_{-0.13}$	$0.07^{+0.25}_{-*}$	$0.03^{+0.14}_{-*}$
$F_{2-10keV}$	$4.36^{+129.64}_{-2.82}$	$4.56^{+1.73}_{-2.10}$	$4.50^{+7.26}_{-*}$
$F^c{}_{10-50keV}$	$1.15^{+1.65}_{-*}$	$1.12^{+0.06}_{-0.52}$	$1.11^{+0.08}_{-0.64}$
$L_{2-10keV}$	$9.48^{+11.06}_{-5.71}$	$5.33^{+4.14}_{-2.82}$	$11.29^{+27.28}_{-*}$
$L_{10-50keV}$	$19.10^{+22.31}_{-11.50}$	$8.04^{+6.23}_{-4.26}$	$12.33^{+29.80}_{-*}$

Notes. We summarise here the best-fits of joint *Swift*-XRT–*NuSTAR* spectra using different torus models at 0.8-50 keV, referred in Section 4.3. The statistics and degrees of freedom for each fit are also reported. The parameters are reported as in Table 2 if not mentioned otherwise. $^a C_{Ins_1} = C_{FPMA/XRT}$ is the cross-calibration constant between *NuSTAR* observation of 2019 and *Swift*-XRT. $^b C_{Ins_2} = C_{FPMA/XRT}$ is the cross-calibration constant between *NuSTAR* observation of 2020 and *Swift*-XRT. ^{c}Flux between 10–50 keV in 10^{-11} erg cm^{-2} s^{-1}.

Table A.3. Summary of best-fit solutions of XMM-Newton and NuSTAR data using different models for NGC 1106

Model	MyTorus Edge-on	MyTorus Face-on	borus02
χ^2/dof	357/295	310/295	304/293
$C_{Ins_1}{}^a$	$0.75^{+0.15}_{-0.14}$	$1.05^{+0.22}_{-0.19}$	$1.07^{+0.24}_{-0.19}$
$C_{Ins_2}{}^b$	$0.92^{+0.15}_{-0.17}$	$1.28^{+0.27}_{-0.22}$	$1.29^{+0.28}_{-0.23}$
Γ	$1.40^{+0.00}_{-*}$	$1.68^{+0.11}_{-0.22}$	$1.92^{+0.44}_{-0.35}$
C_{Tor}	—	—	$0.87^{+0.11}_{-0.24}$
$\theta_{\rm Inc}$	—	—	37^{+37}_{-9}
$N_{H,z}$	$4.00^{+1.73}_{-0.65}$	$3.43^{+*}_{-0.76}$	$4.79^{+*}_{-1.96}$
$N_{H,S}$	$1.46^{+0.18}_{-0.12}$	$7.98^{+*}_{-3.48}$	$4.83^{+*}_{-1.38}$
f_s 10^{-2}	$0.71^{+0.26}_{-0.19}$	$0.72^{+0.71}_{-0.36}$	$0.46^{+1.04}_{-0.38}$
kT	$0.97^{+0.17}_{-0.11}$	$1.01^{+0.47}_{-0.11}$	$0.99^{+0.32}_{-0.12}$
kT	$0.38^{+0.57}_{-0.31}$	$0.42^{+0.21}_{-0.10}$	$0.42^{+0.21}_{-0.11}$
$F_{2-10keV}$	$2.73^{+94.62}_{-2.70}$	$2.63^{+1.87}_{-2.22}$	$2.60^{+11.20}_{-2.45}$
$F_{10-50keV}$	$7.62^{+23.18}_{-7.61}$	$7.83^{+3.02}_{-7.59}$	$7.98^{+11.97}_{-7.97}$
$L_{2-10keV}$	$6.87^{+1.91}_{-1.66}$	$3.68^{+1.58}_{-0.95}$	$5.02^{+5.75}_{-3.97}$
$L_{10-50keV}$	$18.04^{+5.01}_{-4.37}$	$6.16^{+2.65}_{-1.60}$	$5.50^{+6.29}_{-4.35}$

Notes. We summarise here the best fits of joint *XMM-Newton–NuSTAR* spectra using different torus models at 0.6-50 keV, referred to in Section 4.4. The statistics and degrees of freedom for each fit are also reported. The parameters are reported as in Table 2 if not mentioned otherwise. $^a C_{Ins} = C_{FPMA/PN}$ is the cross-calibration constant between *NuSTAR* observation of 2020 and *XMM-Newton* observation of 2019. $^b C_{Ins} = C_{FPMA/PN}$ is the cross-calibration constant between *NuSTAR* observation of 2020 and *XMM-Newton* observation of 2019.

Table A.4. Summary of best-fit solutions of Chandra and NuSTAR data using different models for ESO406-G004

Model	MyTorus Edge-on	MyTorus Face-on	borus02
C-Stat/dof	84/86	84/86	83/84
$C_{Ins_1}{}^a$	$0.73^{+0.65}_{-0.30}$	$0.85^{+0.63}_{-0.36}$	$0.68^{+0.60}_{-0.07}$
$C_{Ins_2}{}^b$	$0.35^{+0.32}_{-0.15}$	$0.41^{+0.31}_{-0.18}$	$0.34^{+0.35}_{-0.06}$
Γ	$1.48^{+0.30}_{-*}$	$1.40^{+0.62}_{-*}$	$1.42^{+0.02}_{-*}$
C_{Tor}	—	—	0.10^{+*}_{-*}
$\theta_{\rm Inc}$	—	—	18^{+69}_{-*}
$N_{H,z}$	$0.85^{+0.43}_{-0.23}$	$0.73^{+0.27}_{-0.14}$	$0.79^{+0.04}_{-0.12}$
$N_{H,S}$	$0.49^{+1.11}_{-0.36}$	$1.30^{+0.73}_{-1.19}$	$4.97^{+*}_{-4.80}$
f_s 10^{-2}	$0.65^{+1.33}_{-0.62}$	$0.81^{+1.29}_{-*}$	$0.37^{+0.65}_{-*}$
kT	$0.51^{+0.20}_{-*}$	$0.52^{+0.19}_{-*}$	$0.52^{+0.18}_{-0.18}$
$F_{2-10keV}$	$3.41^{+1.37}_{-3.41}$	$3.19^{+5.52}_{-3.19}$	$3.56^{+3.47}_{-3.56}$
$F_{10-50keV}$	$3.50^{+0.19}_{-3.50}$	$3.61^{+10.58}_{-*}$	$3.56^{+5.54}_{-3.56}$
$L_{2-10keV}$	$6.77^{+8.68}_{-3.87}$	$3.97^{+26.51}_{-1.71}$	$6.47^{+0.42}_{-0.37}$
$L_{10-50keV}$	$15.58^{+19.96}_{-8.91}$	$10.27^{+68.51}_{-4.44}$	$16.55^{+1.07}_{-0.93}$

Notes. We summarise here the best-fits of joint *Chandra–NuSTAR* spectra using different torus models at 0.7-50 keV, referred to in section 4.5. The statistics and degrees of freedom for each fit are also reported. The parameters are reported as in Table 2 if not mentioned otherwise. $^a C_{Ins_1} = C_{FPMA/ACIS}$ is the cross-calibration constant between *NuSTAR* observation of 2016 and *Chandra* observation of 2012. $^b C_{Ins_2} = C_{FPMA/ACIS}$ is the cross-calibration constant between *NuSTAR* observation of 2020 and *Chandra* observation of 2012.

Table A.5. Summary of best-fit solutions of *XMM-Newton*, *Chandra*, and NuSTAR data using different models for 2MASX J20145928+2523010

Model	MyTorus Edge-on	MyTorus Face-on	borus02
χ^2/dof	545/581	545/581	564/580
$C_{Ins_1}{}^a$	$1.98^{+0.16}_{-0.15}$	$1.98^{+0.16}_{-0.15}$	$1.98^{+0.15}_{-0.15}$
$C_{Ins_2}{}^b$	$1.32^{+0.08}_{-0.08}$	$1.32^{+0.08}_{-0.08}$	$1.31^{+0.08}_{-0.08}$
$C_{Ins_3}{}^c$	$1.95^{+0.16}_{-0.15}$	$1.95^{+0.16}_{-0.15}$	$1.94^{+0.14}_{-0.15}$
Γ	$1.79^{+0.10}_{-0.10}$	$1.77^{+0.11}_{-0.08}$	$1.52^{+0.04}_{-0.05}$
C_{Tor}	—	—	$1.00^{+*}_{-0.23}$
$\theta_{\rm Inc}$	—	—	18^{+*}_{-*}
$N_{H,z}{}^d$	$2.02^{+0.17}_{-0.16}$	$2.04^{+0.19}_{-0.15}$	$2.18^{+0.11}_{-0.13}$
$N_{H,S}{}^e$	$11.93^{+3.85}_{-2.86}$	$20.15^{+8.51}_{-6.33}$	$17.63^{+4.05}_{-4.75}$
f_s 10^{-2}	$0.68^{+0.40}_{-0.39}$	$0.42^{+0.44}_{-*}$	$1.06^{+0.40}_{-0.43}$
$F^f{}_{2-10keV}$	$1.83^{+0.04}_{-0.06}$	$1.83^{+0.05}_{-0.08}$	$1.81^{+0.04}_{-0.09}$
$F_{10-50keV}$	$5.04^{+0.21}_{-0.45}$	$5.07^{+0.46}_{-0.52}$	$6.81^{+0.41}_{-0.53}$
$L_{2-10keV}$	$6.27^{+1.09}_{-0.93}$	$5.95^{+1.18}_{-0.89}$	$8.20^{+0.70}_{-0.64}$
$L_{10-50keV}$	$8.76^{+1.53}_{-1.31}$	$8.52^{+1.69}_{-1.27}$	$17.57^{+1.50}_{-1.37}$

Notes. We summarise here the best-fits of joint *XMM-Newton* , *Chandra* and *NuSTAR* spectra using different torus models at 0.6-50 keV, referred to in Section 4.6. The statistics and degrees of freedom for each fit are also reported. The parameters are reported as in Table 2 if not mentioned otherwise. $^a C_{Ins_1} = C_{ACIS/PN}$ is the cross-calibration constant between *Chandra* observation of 2018 and *XMM-Newton* observation of 2017. $^b C_{Ins_2} = C_{FPMA/PN}$ is the cross-calibration constant between *NuSTAR* observation of 2017 and *XMM-Newton* observation of 2017. $^c C_{Ins_3} = C_{FPMA/PN}$ is the cross-calibration constant between *NuSTAR* observation of 2020 and *XMM-Newton* observation of 2017. ^{d}'Line of sight' column density in 10^{22} cm^{-2}. ^{e}Average column density from scattering in 10^{22} cm^{-2}. ^{f}Flux between 2 and 10 keV in 10^{-12} erg cm^{-2} s^{-1}.

Table A.6. Summary of best-fit solutions of XMM-Newton and NuSTAR data using different models for ESO138-G001

Model	MyTorus Edge-on	MyTorus Face-on	borus02
χ^2/dof	2636/1818	2566/1818	2419/1816
$C_{Ins_1}{}^a$	$1.15^{+0.04}_{-0.04}$	$1.15^{+0.05}_{-0.05}$	$1.16^{+0.03}_{-0.05}$
$C_{Ins_2}{}^b$	$1.07^{+0.04}_{-0.04}$	$1.08^{+0.04}_{-0.04}$	$1.09^{+0.03}_{-0.05}$
Γ	$1.53^{+0.05}_{-0.05}$	$1.66^{+0.03}_{-0.05}$	$1.98^{+0.01}_{-0.03}$
C_{Tor}	—	—	$0.80^{+0.03}_{-0.12}$
$\theta_{\rm Inc}$	—	—	18^{+*}_{-*}
$N_{H,z}$	$0.33^{+0.02}_{-0.02}$	$0.34^{+0.01}_{-0.02}$	$0.47^{+0.07}_{-0.06}$
$N_{H,S}$	$1.47^{+0.60}_{-0.49}$	$3.00^{+0.37}_{-0.55}$	$10.35^{+0.08}_{-0.08}$
Fe $K_\alpha{}^c$	$6.42^{+0.00}_{-0.01}$	$6.42^{+0.00}_{-0.01}$	$6.44^{+0.01}_{-0.01}$
Fe K_α norm^d 10^{-5}	$2.28^{+0.10}_{-0.11}$	$1.91^{+0.11}_{-0.10}$	$1.04^{+0.10}_{-0.13}$
f_s 10^{-2}	$7.46^{+1.07}_{-0.94}$	$8.14^{+0.67}_{-0.87}$	$3.22^{+0.10}_{-0.24}$
kT	$0.68^{+0.01}_{-0.01}$	$0.68^{+0.01}_{-0.01}$	$0.74^{+0.01}_{-0.01}$
$F^e{}_{2-10keV}$	$2.25^{+0.04}_{-0.07}$	$2.24^{+0.04}_{-0.05}$	$2.24^{+0.11}_{-0.27}$
$F^f{}_{10-50keV}$	$1.42^{+0.03}_{-0.11}$	$1.44^{+0.03}_{-0.09}$	$1.43^{+0.06}_{-0.09}$
$L_{2-10keV}{}^g$	$11.59^{+2.25}_{-1.88}$	$12.11^{+0.95}_{-2.04}$	$3.61^{+0.30}_{-0.94}$
$L_{10-50keV}{}^h$	$24.51^{+4.75}_{-3.97}$	$20.90^{+1.65}_{-3.52}$	$3.34^{+0.28}_{-0.87}$

Notes. We summarise here the best-fits of joint *XMM-Newton–NuSTAR* spectra using different torus models at 0.6-50 keV, referred to in Section 4.7. The statistics and degrees of freedom for each fit are also reported. The parameters are reported as in Table 2 if not mentioned otherwise. $^a C_{Ins_1} = C_{FPMA/PN}$ is the cross-calibration constant between *NuSTAR* observation of 2016 and *XMM-Newton* observation of 2013. $^b C_{Ins_2} = C_{FPMA/PN}$ is the cross-calibration constant between *NuSTAR* observation of 2020 and *XMM-Newton* observation of 2013. ^{c}Energy of the Iron K_α line in keV. ^{d}Normalization of line component depicting total photons in cm^{-2} s^{-1}. ^{e}Flux between 2 and 10 keV in 10^{-12} erg cm^{-2} s^{-1}. ^{f}Flux between 10 and 50 keV in 10^{-11} erg cm^{-2} s^{-1}. ^{g}Intrinsic luminosity between 2 and 10 keV in 10^{41} erg s^{-1}. ^{h}Intrinsic luminosity between 2 and 10 keV in 10^{41} erg s^{-1}.

Appendix B: Figures of X-Ray Spectra

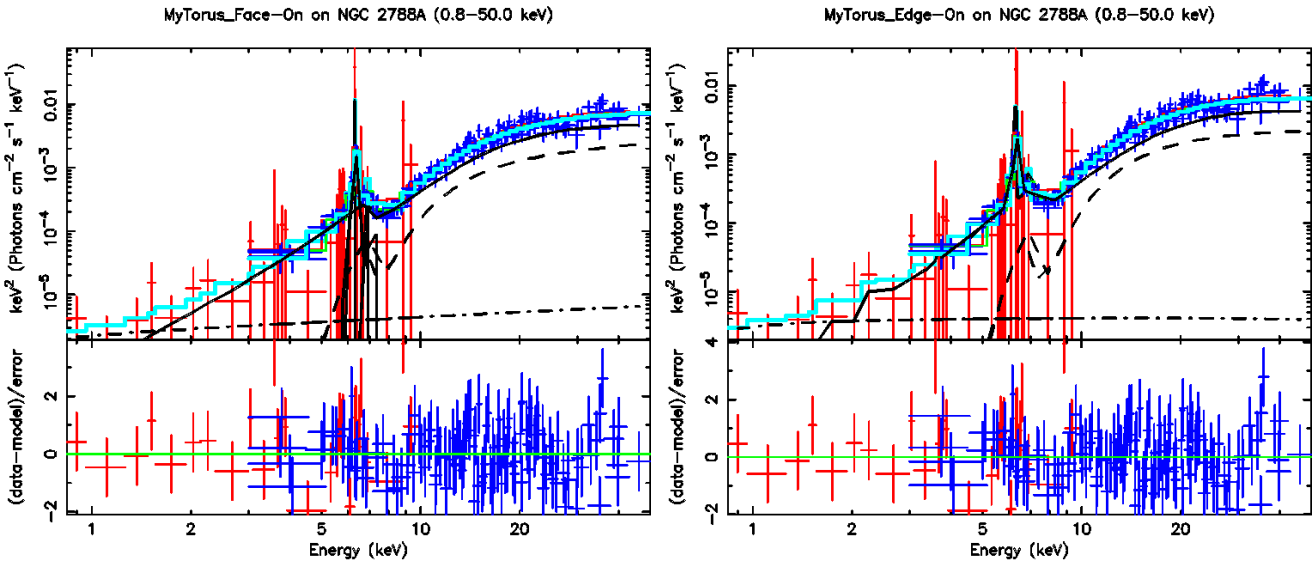

Fig. B.1. Same as Figure 1, for NGC 2788A, without mekal.

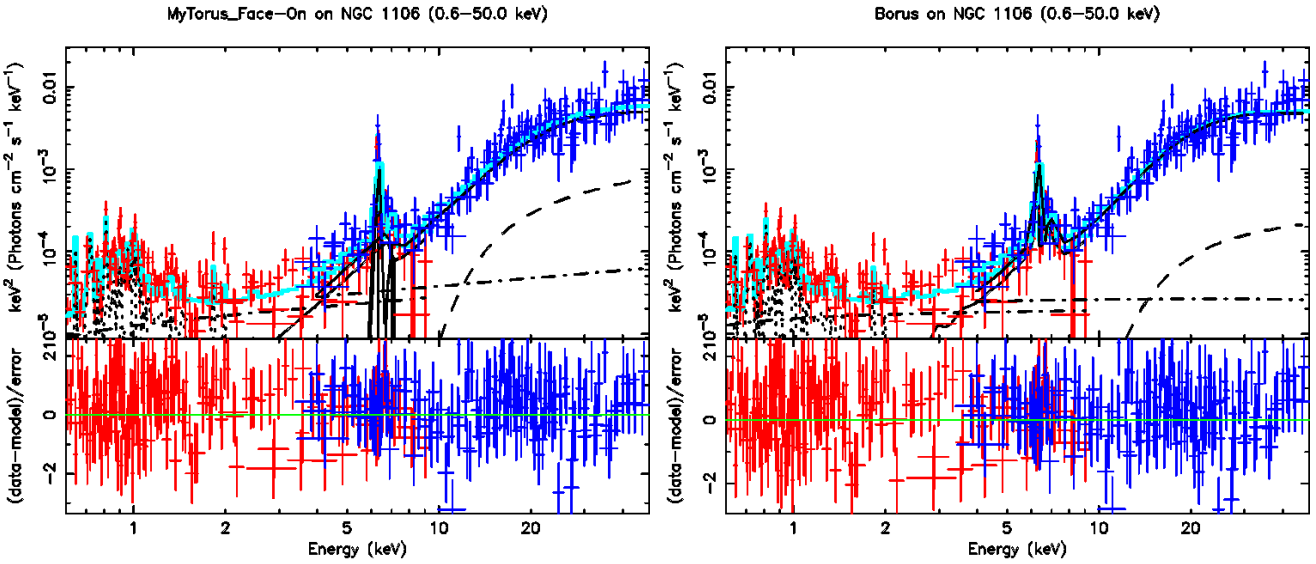

Fig. B.2. Same as Figure 1, for NGC 1106.

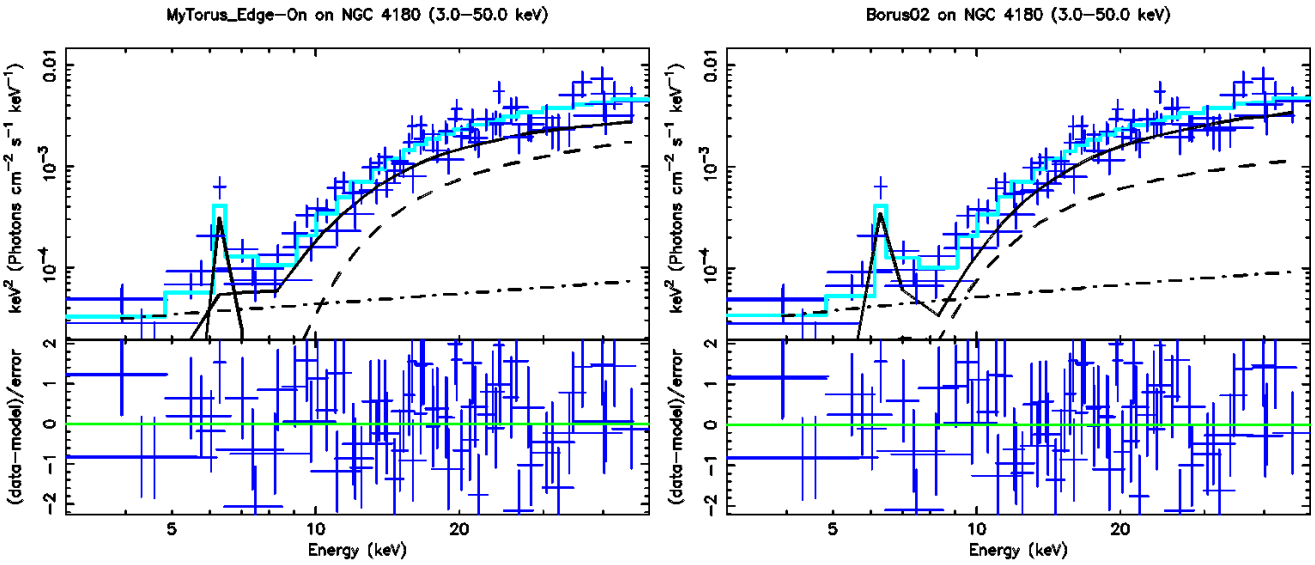

Fig. B.3. Same as Figure 1, for NGC 4180, without any soft X-ray points and mekal.

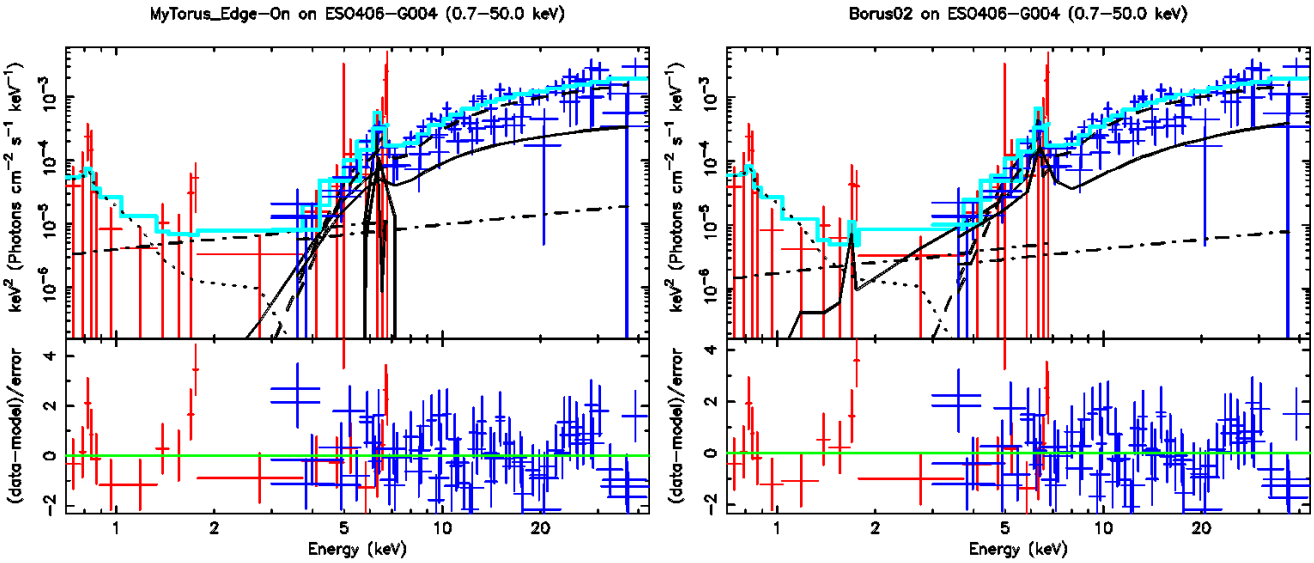

Fig. B.4. Same as Figure 1, for ESO406-G004.

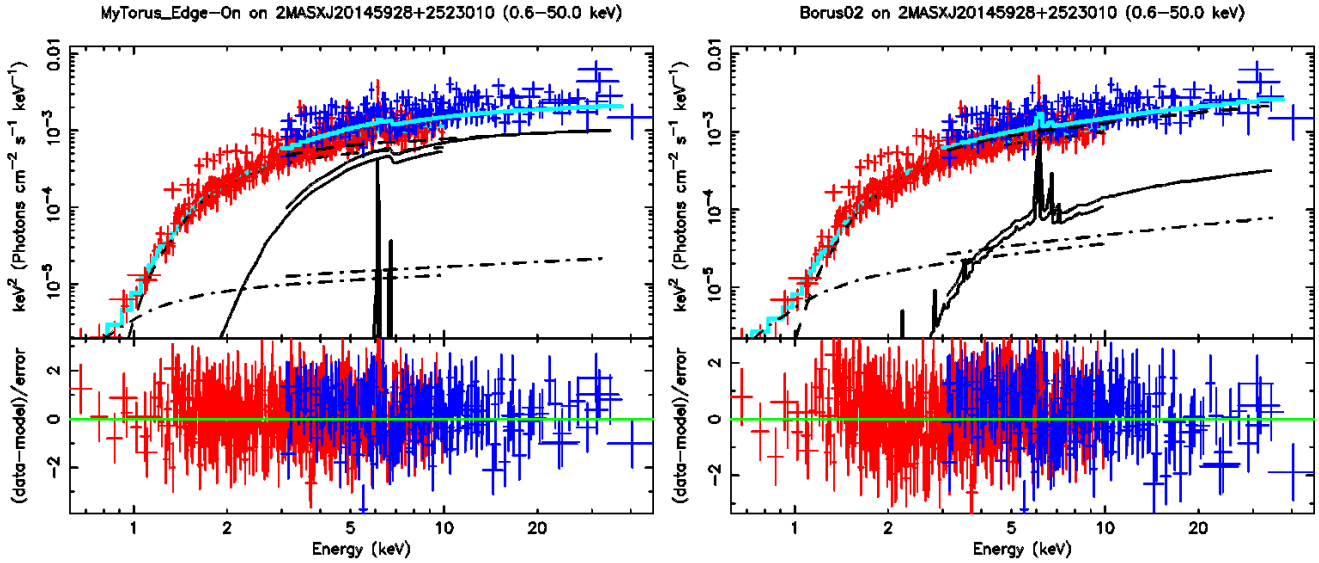

Fig. B.5. Same as Figure 1, for 2MASXJ20145928+2523010, without mekal.

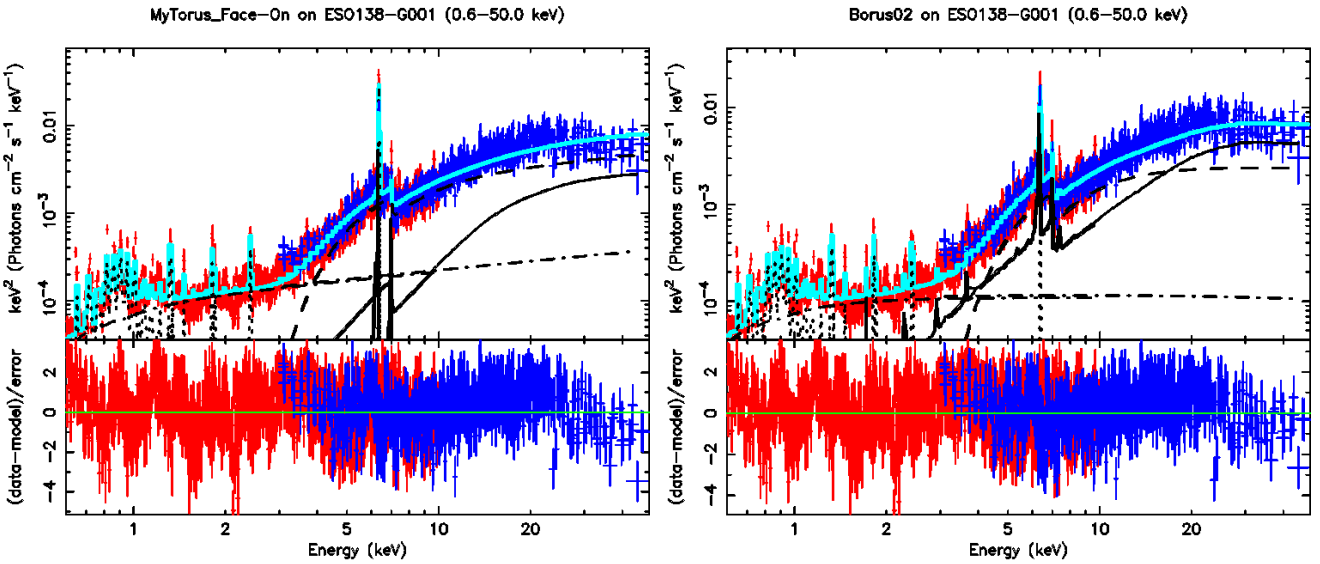

Fig. B.6. Same as Figure 1, for ESO138-G001, with extra four Gaussian line profiles (dot).